Paper IV

Thermochronological history of an orogen-passive margin system - an example from N Mozambique

Emmel, B., Kumar, R., Ueda, K., Jacobs, J., Daszinnies, M., Thomas, R.J., Matola R.

IV

Thermochronological history of an orogen-passive margin system – an example from NE Mozambique

B. Emmel[a,*], R. Kumar[a], K. Ueda[a], J. Jacobs[a], M.C. Daszinnies[b], R.J. Thomas[c], R. Matola[d]

[a]*Department of Earth Science, University of Bergen, Allégaten 41, 5007 Bergen, Norway*
[b]*SINTEF Petroleum and Energy, Basin Modelling Group, No-7465 Trondheim, Norway*
[c]*British Geological Survey, Nicker Hill, Keyworth, Nottingham NG12 5GG, UK*
[d]*Direcção Nacional de Geologia(DNG), Maputo, Mozambique*

Abstract

Abstract In this paper, we present a conceptual model to describe the post Pan-African ($< \sim$500 Ma) basement cooling pattern for NE Mozambique. The cooling history is derived from combined low-temperature thermochronological dating methods comprising titanite, zircon and apatite fission track (FT) data. After Pan-African orogenesis ($\sim$620-530 Ma) the Precambrian basement was subject to extensional tectonics and a relatively slow Lower Ordovician to Recent cooling with rates of $\sim$2.2 to 0.1 °C Myr^{-1}. Basement rock cooling was mainly a response to Late Palaeozoic to Mesozoic rifting between northern Mozambique and East Gondwana during the opening of the Rovuma and Mozambique sedimentary basins. Meanwhile, different dynamic margin and basin types evolved along the eastern and southern continental margins of NE Mozambique. During the Late Carboniferous-Triassic an intracontinental rift opened between NE Mozambique and East Antarctica and the fastest denudation was focused along the present southern continental margin. Since the Middle Jurassic, tectonic denudation along the Rovuma margin was localised in a narrow zone, some 30 km wide, associated with erosion along strike-slip faults. In contrast, the Jurassic-Cretaceous opening and ocean crust formation in the Mozambique Basin was accompanied with an unusually uniform Late Cretaceous cooling pattern over a large area ($\sim$150 000 km2) of the basin hinterland. This pattern can be explained by isostatic and erosional response to magmatic underplating or differential stretching, whereby the old Pan-African lithospheric structure appears to have important controls on later events.

Keywords: Thermochronology 1140, Continental margins: divergent 8105, Continental tectonics: general 8110, Continental margins: transform 8106, Tectonics and landscape evolution 8175, Africa 9305

1. Introduction

On a global scale, many passive margins are located within crustal segments which were deformed by compressive tectonics and crustal thickening in their geological past. These margin types can be referred as "orogen – passive continental margin systems". In such systems, older orogenic structural anisotropies were reactivated during the later passive margin formation. Consequently, inherited structures may have a dominant control on continental break-up kinematics [e.g. Cox, 1992; Daly et al., 1989]. Nevertheless, the correlation between early, orogen-related structures and the post-orogenic thermo-tectonic evolution during continental break-up has not been sufficiently studied and documented. This paper describes the thermo-tectonic history of the Precambrian metamorphic basement in northern Mozambique which represents the remnant of a deeply eroded orogen [Viola et al., 2008; Boyd et al., 2010]. Today, the mid to lower crustal roots of the orogen are exposed as metamorphic basement rocks with well defined structural anisotropies such as ductile high strain zones and major shear zones [e.g., Norconsult, 2007; Viola et al., 2008]. The timing of orogenesis in northern Mozambique is documented by numerous geochronological data [Jamal, 2005; Grantham et al., 2008; Jacobs et al., 2008; Viola et al., 2008; Bingen et al., 2009], indicating that collision between Meso- and Neoproterozoic tectonic blocks led to crustal thickening between $\sim$620 and 530 Ma during the "Pan-African" or "East African" Orogeny which led to the final amalgamation of Gondwana (Figure 1a) [Pinna et al., 1993; Meert, 2003; Boger and Miller, 2004; Jacobs and Thomas, 2004; Bingen et al., 2009; Thomas et al., 2010]. The cooling

*Corresponding author: Tlf +47 5558 3516
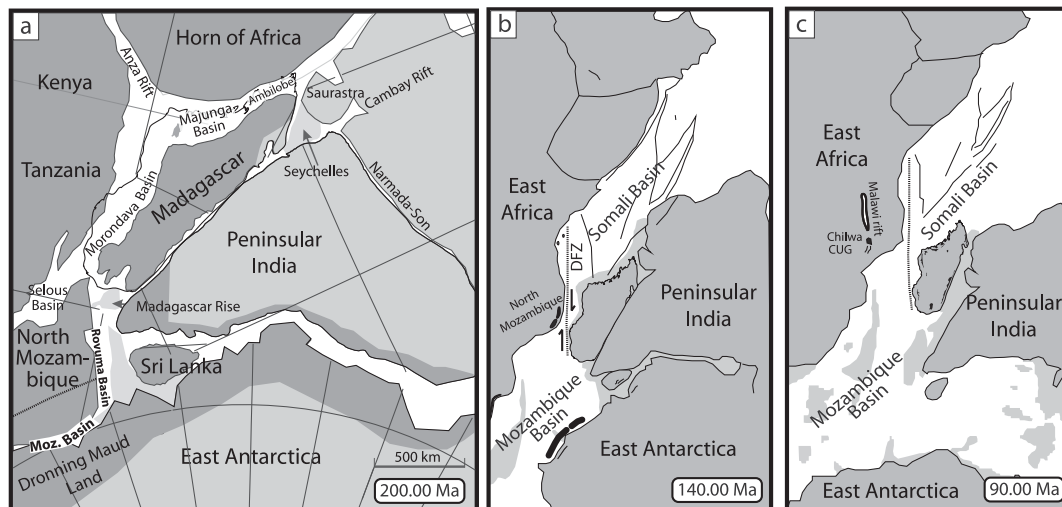*Email address:* benjamin.emmel@geo.uib.no (B. Emmel)

Figure 1: a) Central Gondwana at ∼200 Ma. Basement rocks overprinted during the Pan-African orogenies are shown in dark grey (modified after Reeves et al., 2004; Meert, 2003; Kusky et al., 2003). b, c) Gondwana break up 140 Ma and 90 Ma with Jurassic and Cretaceous volcanic rocks in central Gondwana shown in black [after de Wit 2003; Luttinen and Furnes, 2000; Torsvik et al., 1998; Eby et al., 1995]. Abbreviations: CUG: Chire-Urema Graben; DFZ: Davie Fracture Zone; Moz. Basin: Mozambique Basin.

history during the transition from crustal thickening to crustal thinning has been somewhat constrained by high to medium temperature, Ar-Ar hornblende, biotite and titanite FT data [Daszinnies et al., 2009]. Subsequent extensional tectonics during Gondwana break-up lead to the opening of sedimentary basins (Figure 1b, c) and transform/passive margin formation, as documented from sedimentary rocks in the late Paleozoic- Cenozoic basins [Salman and Abdula, 1995]. The coast of N Mozambique exhibits two distinct margin styles and associated basins. Along the eastern margin of northern Mozambique the N-S elongated Rovuma Basin is a typical transform basin. In contrast, the southern coast is bounded by a passive margin with the Mozambique Basin as the sedimentary sink (Figure 1).

In this paper, we focus on two topics. Firstly, we aim to reconstruct the basement cooling history for the time between the peak orogenic activity in the Neoproterozoic and the opening of the Mesozoic rift basins. To this end the late kinematic Lurio Belt (LB) has been studied in some detail. This prominent WSW-trending structure separates different basement blocks (Figure 2). Secondly, we date and quantify the onshore denudation histories of the two distinctly different margin styles, both of which

formed within the same regional tectonic setting and under similar climatic conditions.

To achieve these objectives we used a combined thermochronological approach using fission track (FT) data from titanite, zircon and apatite. These methods constrain the cooling histories of basement samples from ∼300 °C to 60 °C [e.g. Wagner and van den Haute, 1992 and references therein]. Assuming present surface temperatures of ∼20 °C and a geothermal gradient of 20 ± 5 °C/km they effectively record denudation in the upper ∼11-19 km of the crust, sufficient to record denudation for a multiple rifted margin.

2. Geodynamic setting and geological overview

The geology of northern Mozambique is mainly characterised by basement rocks fringed by Phanerozoic sedimentary basins, namely the onshore Metangula Basin in the NW, the partially onshore Rovuma Basin stretching along the eastern continental margin, and the mainly offshore Mozambique Basin along the southern margin (Figure 2). The main structural event recorded in the metamorphic basement is the Ediacaran to Lower Ordovician ("Pan-African") East-African orogeny during which several crustal blocks were amalgamated to form the
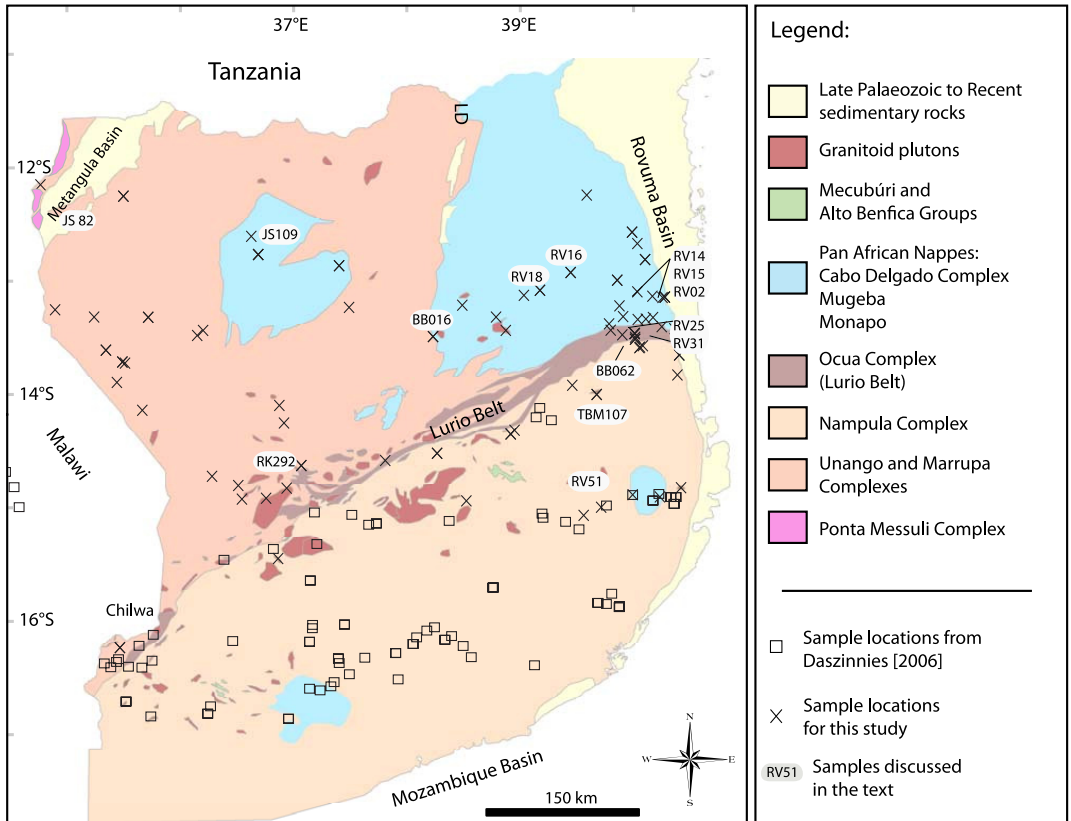
Figure 2: a) Simplified geological overview map of northern Mozambique with locations of dated samples. LD: Lugenda depression.

Gondwana supercontinent [e.g., Stern., 1994; Jacobs and Thomas, 2004; Boyd et al., 2010]. Northern Mozambique lies in the core of this major N-S trending orogenic belt. The main compressional accretionary phase was followed by episodes of extensional tectonics leading ultimately to the formation of sedimentary basins fringing the basement from the Permian onward. During the Permo-Triassic (Karoo), mainly siliciclastic sediments accumulated within intracontinental rift basins such as the Metangula Basin. Extension culminated in Gondwana break-up during Jurassic to Cretaceous times, when oceanic crust was formed between northern Mozambique and East Antarctica/Madagascar and the Mozambique Basin widened. Offshore, between Mozambique and Dronning Maud Land (East Antarctica), Mesozoic magnetic seafloor anomalies (M25-M0) document the drifting of the East Antarctica/Madagascar/India Sychelles block away from East Africa between ∼158-119 Ma [Salman and Abdula, 1995]. The oldest seafloor anomaly M25 (158 Ma) gives the minimum date for the separation between the two continental blocks along the Davie Fracture Zone (Figure 1) and for the opening of the Rovuma and the Mozambique Basin. Since then, the main sedimentary successions of the basins were deposited and the present continental margin was developed [Salman and Abdula, 1995]. The following section is a résumé of the main lithological units of northern Mozambique, with references to detailed studies.

2.1. Metamorphic basement of N Mozambique

The first modern tectono-stratigraphic subdivision of northern Mozambique was published by Pinna et al. [1993]. This was refined following a major World Bank geological mapping project between 2002- 2006 [Norconsult Consortium, 2007; Macey et al., 2007; Engvik et al., 2007; Viola et al., 2008; Bingen et al., 2009; Thomas et al., 2010; Boyd et al., 2010]. According to these authors the region can be subdivided into 7 main lithological complexes which are here reported in a chronological order: The oldest rocks belong to the Ponta Messuli Complex in NW Mozambique (Figure 2). It consists of Palaeoproterozoic amphibolite to granulite facies metaigneous rocks [Bingen et al., 2009]. Younger rocks occur in the southern part of N-Mozambique, where the Nampula Complex (Figure 2) consists of Stenian orthogneisses. In the NE and central part of the studied area the Unango and Marrupa complexes crop out (Figure 2). Both have Stenian – Tonian U-Pb zircon crystallisation ages. The Unango Complex consists mainly of felsic to intermediate orthogneisses. Locally paragneisses crop out between orthogneiss-bodies and metasedimentary rocks of the Ediacaran Geci Group occur in tectonic lenses [Melezhik et al., 2006]. The Marrupa Complex is made up of felsic orthogneisses, paragneisses and metasediments. The Unango, Marrupa and Nampula complexes were metamorphosed during the Pan-African orogeny [Viola et al., 2008] and reached amphibolite to granulite facies metamorphic conditions. All three complexes are intruded by plutons of middle Neoproterozoic to Ordovician ages, which appear to relate to the latest phase of the Pan-African orogeny [see discussions in Grantham et al., 2008; Jacobs et al., 2008; Viola et al., 2008]. The Ocua Complex separates the metamorphic basement into a northern and southern part. It contains granulites, highly sheared gneisses and mylonites and reached granulite facies metamorphism during the Pan-African orogeny [Norconsult Consortium, 2007]. Part of this complex coincides with the most prominent structure, the LB, a ∼600 km SW-NE trending tectonic lineament (Figure 2).

The NE part of the basement exposes the higher structural levels of the Cabo Delgado Nappe Complex [Viola et al., 2008] consisting of a lithological assemblage of granitic, tonalitic, gabbroic, and amphibolitic gneisses as well as various paragneisses, metavolcanic rocks and mafic granulites of mainly Neoproterozoic age. This complex represents a Pan-African transported nappe system [Viola et al., 2008] north of the LB. South of the LB, the Mugeba and Monapo klippen are remnants of corresponding Pan-African nappes overlaying the Nampula Complex (Figure 2). The Mugeba klippe contains charnockitic gneisses, mafic granulites and meta-sedimentary rocks which reached granulite facies conditions [Macey et al.,

2007]. A broad variety of strongly deformed granulitic ortho- and paragneiss, undeformed ultramafic, mafic and felsic rocks partly metamorphosed to amphibolite facies conditions form the Monapo klippe [Macey et al., 2007].

2.2. Phanerozoic Sedimentary Rocks

The oldest Phanerozoic sedimentary rocks are found in the NE-SW trending Metangula Basin located at the NW tip of Mozambique (Figure 2). The Permo-Triassic (Karoo Supergroup) sedimentary rocks include conglomerates, sandstones, mudstones, and coal-bearing seams [Verniers et al., 1989]. The Lugenda depression (Figure 2) east of the Metangula Basin contains similar rocks of the same age [Lächelt, 2004]. Seismic data suggest, that the Rovuma and Mozambique basins also contain Permo-Triassic strata, but onshore outcrops of such rocks are unknown, nor have they been recorded from boreholes [Salman and Abdula, 1995].

2.2.1. Rovuma Basin

The NNW-SSE striking Rovuma Basin extends over ∼470 km south from the northern border of Mozambique with Tanzania. Onshore, the basin outline is wedge-shaped with a maximum onshore width of ∼160 km in the north, thinning to 20 km wide in the south (Figure 2). Maximum thickness for the sedimentary strata is estimated at ∼10 km in southernmost Tanzania [Kent et al., 1971], but the succession thins to ∼1 km in northern Mozambique onshore. The lithostratigraphy of the Rovuma Basin is described in detail by Key et al. [2008] and Smelror et al. [2008].

The oldest sedimentary rocks belong to the Pemba Formation. These are predominantly continental clastic sandstones, marine shale-siltstones and sandstones containing belemnites, bivalves and ammonites. The age of the Pamba Formation is constrained by the bivalve *Megatrigonia schwarzi* and the belemnite *Duvalia Grasiana* to Valanginian to Barremian-Aptian [Civitelli, 1988] or from upper Jurassic to Aptian based on marine microfloras [Smelror et al., 2008]. However, palynological assemblages give a correlation with the *Dinogodinium jurassicum* zone, arguing for a Tithonian to Albian age range [Norconsult Consortium, 2007]. The thickness of the formation has not been accurately determined but it reaches several thousand meters offshore [Key et al., 2008]. The 100 m thick continental siliciclastic rocks of the Rio Mecole and N'Gapa Formations are probably of the same age like the lower Pemba Formation [Key et al., 2008; Smelror et al., 2008]. The overlying Macomia Formation consists of a ∼300 m thick succession of conglomerates and sandstones. Terrestrial and marine palynomorphs indicate a late Aptian–Albian depositional age [Hancox et al., 2002].

Calcareous sandstones and intensely bioturbated marls make up the overlying Mifume Formation [Civitelli, 1988]. A Campanian to middle Maastrichtian age is determined by the occurrence of the foraminifera species *Globotruncana arca*, *Globotruncana ventricosa* and *Globotruncana falsostuarti* [Civitelli, 1988]. It reaches its maximum onshore thickness of 200 m west of Pemba, but a thickness of ~915 m is reported from the Mocimboa-1 borehole where the formation spans the whole of the upper Cretaceous [Salman and Abdula, 1995]. The youngest sedimentary rocks of the Rovuma basin are Eocene to Miocene-Pliocene conglomerates, sandstones, siltstones, mudstones and reef related limestones of the Alto Jingone, Quissanga, Chingda and Mikindani Formations. Onshore, a cumulative thickness of ~250 m has been recorded but offshore these formations attain a total thickness of up to 2000 m [Civitelli and Mariani, 1984; Civitelli, 1988; Salman and Abdula, 1995].

2.2.2. Mozambique Basin

The Mozambique Basin is located south of the basement margin of northern Mozambique (Figure 1). The oldest strata detected from wells are mid Jurassic volcanic rocks and late Jurassic continental red beds [Salman and Abdula, 1995]. In the Zambezi Delta, the sediments of the Mozambique Basin reach a maximum thickness of ~11 km, comprising deep marine to deltaic clastic and carbonacous deposits [Salman and Abdula, 1995]. The sedimentary record of the Zambezi Delta reflects the continuous evolution of a passive continental margin since the Early Cretaceous. Sediment influx peaks are recognized during the Late Cretaceous (90-65 Ma), Oligocene (34-24 Ma) and Late Miocene (10 Ma) which are linked to tectonically-driven enhanced denudation and changes in the catchment size of the delta [Walford et al., 2005].

2.2.3. Mesozoic Igneous Rocks

In northern Mozambique, Mesozoic igneous rocks cross-cutting the metamorphic basement are common along the SE coastal margin and the SW tip of the Malawi rift (Figures 1b, 1c, 2). Dolerites from the SE margin give K-Ar whole rock and Sm-Nd model ages of 180-160 Ma [Jaritz et al., 1977; Grantham et al., 2005]. The fissure-type basalts in the Chire-Urema Graben (Figure 1c) yield K-Ar whole rock ages of 137-115 Ma and are associated with crustal extension in Cretaceous times [Lächelt, 2004; Nairn et al., 1991]. Similarly kimberlites intruding into the Metangula Basin give a Rb-Sr phlogopite age of 141 ± 2 Ma [Key et al., 2007]. In southernmost Malawi thermochronological results are reported from the Chilwa alkaline province (Figure 1c) by Eby et al. [1995]. That study reported K-Ar data ages between ~123 and 111

Ma, titanite FT ages between ~137 and 123 Ma, one zircon FT age of ~98 Ma and apatites FT ages between 94 and 83 Ma. During the Mesozoic, igneous activity was focused on the continental margins of central Gondwana (Figure 1). In southern Africa, the Karoo Large Igneous Province was emplaced between 184-179 Ma [Duncan et al., 1997]. Jurassic continental flood basalts in East Antarctica erupted during a shorter, but similar period between 184 Ma to 175 Ma as revealed by $^{40}Ar/^{39}Ar$ feldspar and/or whole rock ages [Duncan et al., 1997; Zhang et al., 2003]. K-Ar whole rock and $^{40}Ar/^{39}Ar$ biotite ages from dolerite dykes in eastern Sri Lanka range between ~170 and 143 Ma [Takigami et al., 1999; Yoshida et al., 1989]. Volcanic rocks from the eastern and western margins of Madagascar (Figure 1c) have been dated at ~91-86 Ma by $^{40}Ar/^{39}Ar$ whole-rock step heating and the laser fusion method on single and multiple feldspar grains and are thought to be associated with hot spot activity [Storey et al., 1995].

3. Methods

Apatite, zircon and titanite separates, (grain sizes of $\leq$ 315 μm) were extracted from samples using conventional preparation techniques including crushing, sieving, Wilfley table, heavy liquid and magnetic separation. Apatite and titanite grains were embedded in epoxy resin, while zircons were embedded in Teflon. All were then ground and polished to expose internals crystal surfaces. The apatite fission tracks were revealed by etching polished mounts with 5 M HNO_3 for 20 s, zircons in a concentrated NaOH/KOH (8:12) eutectic melt at a temperature of 225 °C in closed Teflon beakers with etching timed between 10 and 26 hours, and the titanites were etched individually for 17-22 min in a mixture of concentrated HF, HNO_3, HCl and H_2O (1:2:3:6) at temperatures of 20-21 °C. Induced tracks were recorded with uranium-free mica detectors following the external detector approach [Gleadow, 1981] and revealed after irradiation by exposing the micas for 15 min to 40 % HF etching at 20-21 °C. Fission track sample mounts were irradiated at the FRM II research reactor facility in Munich-Garching (Germany) using a total thermal neutron fluence of $\sim 0.5 \cdot 10^{16} ncm^{-2}$ for titanite and zircon and $1 \cdot 10^{16} ncm^{-2}$ for apatite irradiations. CN2 (titanite and zircon) and IRMM 540 (apatite) dosimeter glasses were used to monitor a neutron fluence gradient. The track densities, length and etch pit diameter parameters (D_{par}) were determined using the conventional external detector method at a magnification of $1250x$ and of $2000x$ in transmitted and reflected light. We used a Olympus BX51 microscope equipped with a drawing tube, a Kintec® stage and a Calcomp® digitizer with the latter two being operated by the FT-Stage software
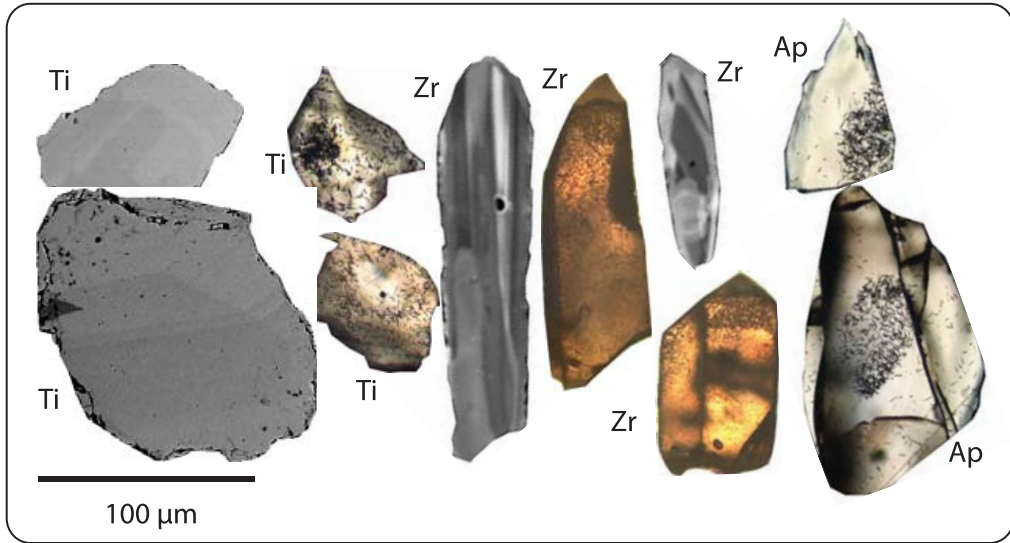
Figure 3: Representative examples for zoned titanites, zircons and apatites, shown as backscatter electron and cathodoluminescence images and after etching for fission track analyses. Complex uranium zoning characterised by different degrees of luminescence and fission track densities of these minerals can lead to an extra error, not governed by a Poisson distribution and can cause failure of the χ^2 test for fission track densities.

[Dumitru, 1991]. Apatite grains alone, exposing internal surfaces parallel to the crystallographic c-axis were used for track density and track length measurements. Five etch pits per grain dated and three etch pits per crystal used for track length measurement were measured. Arithmetic mean D_{par} values were used for each grain and measured track. Titanite, zircon and apatite FT central ages were calculated according to the zeta calibration method [Hurford, 1990]. Throughout this study FT, age errors are quoted at the 1σ confidence level and were derived by the conventional method [Green, 1981]. The closing temperature of the titanite FT system is estimated to be 275 $\pm$ 25 °C [Kohn et al., 1993]. In-situ observations at the deep continental drill hole "Kontinentale Tiefbohrung" in Germany give an estimate for the partial annealing zone (PAZ) of the titanite FT system between 310 to 265 $\pm$ 10 °C [Coyle and Wagner, 1998]. For the zircon FT system, different closing temperatures are reported [e.g., Wagner and Van den Haute, 1992; Brandon et al., 1998; Rahn et al., 2004] but they range in general from 250 to 175 °C [Harrison et al., 1979] and for slowly cooled rocks a closure temperature of < 205 °C can be estimated [Bernet, 2009]. The PAZ of the apatite FT system is constrained to a temperature range between 110 $\pm$ 10 °C and 60 °C

[Green et al., 1986a, b; Wagner and van den Haute, 1992 and references therein]. The apatite FT data, including single grain apatite FT ages, track lengths, lengths angles to crystallographic c-axis, etch pit diameters and standard deviations, were used to model specific hypothetical time-Temperature (t-T) paths. An inverse modeling procedure, using the program "HeFTy" [Ketcham, 2005], was carried out applying the annealing algorithm of Ketcham et al. [1999]. Etch pit diameter (D_{par}) values served as a kinetic parameter. If a sample failed the χ^2-test we used two populations defined by the single grain age and track length specific D_{par} values. Note, that the model precision increases with the amount of dated grains and measured track lengths. The apatite FT modeling procedure was constrained by the following external t-T parameters:

a) The titanite and zircon FT ages give the starting conditions. If these data were not available the locally closest titanite and zircon FT ages were chosen.

b) Depositional ages of adjacent sedimentary units indicate that the samples were near the surface.

c) A present surface temperature of ∼20 °C is the final modeling constraint.

Sample	E-Long. [Dec. °]	S-Lat. [Dec. °]	Elev. [m]	Lithology	Mineral (# Gr.)	ρ_s [$\frac{10^5}{cm^{-3}}$]	N_s (#)	ρ_i [$\frac{10^5}{cm^{-3}}$]	N_i (#)	ρ_d [$\frac{10^5}{cm^{-3}}$]	N_d (#)	χ^2 [%]	C. Age ±1σ [Ma]	MTL ±1σ [μm]	S_D (# TL)	D_{par} [μm]
North of the Lurio Belt																
JS82	34.761	-12.139	506	Granite	Zr (21)	119.44	1982	45.14	749	18.70	8333	0.1	285.1 ±19.6	-	-	-
JS304	39.577	-12.230	309	Granodioritic gneiss	Ap (18)	2.93	80	6.42	175	15.77	9497	97.9	90.4 ±12.6	-	-	2.12
RK106	35.493	-12.240	926	Leucogranite	Ti (5)	72.76	201	23.17	64	20.17	6809	0.1	438.9 ±120.2	-	-	-
RK11/471	35.144	-12.423	729	Syenitic gneiss	Ap (8)	61.78	325	61.40	323	16.19	6652	65.5	193.3 ±18.8	-	-	2.37
TBM138	39.978	-12.559	233	Granitic gneiss	Ap (8)	17.75	318	16.69	299	18.97	9823	60.9	238.6 ±23.5	-	-	1.81
					Ti (20)	132.56	1497	53.40	603	21.36	6809	88.8	360.9 ±19.6	-	-	-
JS109	36.620	-12.597	-	Enderbite	Ap (9)	1.87	87	3.10	144	16.25	6652	83.4	117.3 ±17.3	-	-	1.51
TBM139	40.024	-12.660	168	Granitic gneiss	Ap (15)	24.10	515	17.78	380	16.28	6652	30.4	260.6 ±23.4	10.80±0.20	2.01 (100)	2.13
RK117	36.681	-12.757	493	Tonalitic gneiss	Ap (20)	5.11	560	8.24	903	17.22	9823	8.4	127.3 ±11	-	-	1.56
					Ti (20)	37.16	1641	8.69	384	20.23	6809	55.8	578.4 ±36	-	-	-
					Ti (20)	76.03	2087	20.26	556	17.88	8333	99.1	385.5 ±21.0	-	-	-
					Ti (23)	3.32	163	2.52	124	16.27	6652	9.7	254.5 ±40.5	-	-	3.07
JS309	40.093	-12.802	323	Granodioritic gneiss	Zr (27)	178.14	1984	81.80	911	18.68	8333	78.7	236.5 ±11.4	-	-	-
BB007	37.395	-12.857	417	Granitic gneiss	Ap (19)	12.89	1121	20.09	1747	17.28	9823	30.6	132 ±9.3	-	-	1.67
					Ti (23)	41.89	899	16.31	350	21.19	6809	0.6	374.1 ±34	-	-	-
RV16	39.437	-12.917	456	Syenite	Ap (19)	12.61	591	17.12	802	16.16	6652	23.3	144.1 ±12.5	-	-	1.98
					Ti (16)	93.81	877	41.18	877	19.78	6809	0.2	309.7 ±30	-	-	-
RV20	39.847	-12.985	304	Bt-gneiss	Ap (19)	10.64	872	19.31	1582	19.31	4911	0.0	128 ±11.9	12.37 ±0.17	1.54 (82)	2.15
					Ti (8)	45.55	450	18.83	186	19.89	6809	16.4	326.8 ±39.3	-	-	-
RV18	39.165	-13.075	489	Granitic gneiss	Ap (27)	7.12	934	13.51	1772	15.61	9497	74.2	103 ±5.6	-	-	2.20
					Ti (20)	63.05	1293	26.57	545	19.83	6809	48.4	320.9 ±19	-	-	-
RV15	40.024	-13.089	296	Bt-gneiss	Ap (21)	14.58	1595	26.47	2896	18.27	4911	0.0	121.3 ±10.5	11.74±0.15	1.54 (100)	2.05
RV17	39.024	-13.119	507	Bt-gneiss	Ap (16)	35.65	1929	52.07	2817	19.11	4911	1.1	158.1 ±11.2	13.34±0.13	1.31 (100)	2.20
RV14	40.157	-13.128	234	Gabbro	Ap (11)	9.84	483	17.65	866	19.23	4911	0.0	128 ±17.4	-	-	2.01
RV2C	40.267	-13.134	173	Granitic gneiss	Ap (20)	13.18	1198	19.80	1800	19.06	4911	11.4	151 ±11.2	13.61±0.12	1.16 (100)	2.48
RV01	40.267	-13.135	168	Syenite	Ap (11)	5.76	218	9.59	363	15.61	9497	71.3	117.2 ±10.9	-	-	2.31
					Ti (23)	58.15	1907	46.74	549	19.55	6809	8.1	453.8 ±28.4	-	-	-
RV12	40.246	-13.139	183	Syenite	Ap (22)	1.75	164	2.48	232	15.61	9497	71.3	137.7 ±15	-	-	2.21
					Ap (13)	4.06	226	2.93	163	18.72	4911	81.8	305.4 ±36	11.52±0.39	1.89 (24)	2.18
BB024	38.481	-13.207	574	Banded granulite	Zr (13)	131.48	1028	66.12	517	18.49	8333	82.6	214 ±12.9	-	-	-
OC15	39.866	-13.213	232	Bt-gneiss	Ap (21)	10.22	880	21.13	1820	15.61	9497	63.5	94.6 ±5.2	13.27±0.11	1.15 (101)	2.11
BB002	37.482	-13.226	738	Granitic gneiss	Ap (19)	4.35	404	3.53	328	18.46	9823	63.4	268.3 ±25.1	-	-	1.96
TBM021	34.890	-13.248	878	Hbl-px gneiss	Ap (9)	10.20	176	6.72	116	18.29	9823	88.5	326 ±43.2	-	-	3.95
ONOK432	35.235	-13.312	-	Quartz monzonite	Ap (17)	28.36	753	33.90	900	15.61	9497	83.2	162.7 ±10	-	-	2.06
AS0421	38.779	-13.313	564	Granitic gneiss	Ap (17)	13.72	466	17.57	597	16.09	6652	8.9	151.4 ±14	-	-	1.83
RS302	35.712	-13.314	1071	Granitic gneiss	Zr (23)	141.52	3431	59.40	1440	18.75	8333	69.5	259.2 ±10.7	-	-	-

Table 1: Fission track results. For the titanite and zircon FT ξ-calibration we used the Fish Canyon Tuff and Mount Dromedary age standards. The personal apatite FTξ-values were calibrated against the Fish Canyon and Durango age standards (e.g., Hurford, 1990). Ages are calculated using dosimeter glasses: ξ_{CN2} (titanite and zircon), $\xi_{IRMM-540}$ (apatite) with $\xi_{CN2}=118 \pm 3$ (titanite, Emmel), $\xi_{CN2}=140 \pm 3$ (zircon, Kumar), $\xi_{IRMM-540}=241 \pm 13$ (apatite, Emmel) and $\xi_{IRMM-540}=252 \pm 9$ (apatite, Kumar). Fission track (FT) ages are reported as central ages. ρ_s, ρ_i, ρ_d, N_s, N_i, N_d: densities and number (#) of counted spontaneous, induced and dosimeter glass tracks, C. Age: Central FT age, 1σ: one sigma error, χ^2: Chi-square probability, MTL: mean track length; SD: standard deviation; D_{par}: mean etch pit diameter.

Sample	E-Long. [Dec.°]	S-Lat. [Dec.°]	Elev. [m]	Lithology	Mineral (# Gr.)	ρ_s $[10^5 cm^{-2}]$	N_s (#)	ρ_i $[10^5 cm^{-2}]$	N_i (#)	ρ_d $[10^5 cm^{-2}]$	N_d (#)	χ^2 [%]	C. Age $\pm1\sigma$ [Ma]	MTL $\pm1\sigma$ [μm]	S_D (# TL)	D_{par} [μm]
RV25	40.162	-13.317	242	Bt-gneiss	Ap (21)	10.82	438	11.39	461	16.25	6652	93.5	183.5±16.1	-	-	1.89
RV24	40.099	-13.330	243	Granitic gneiss	Ap (19)	13.41	1022	13.41	1494	18.67	4911	33.9	152.1±10.1	12.94±0.17	1.18 (100)	2.15
OC14	39.776	-13.374	340	Migmatitic gneiss	Ap (21)	20.57	1055	41.35	2121	15.61	9497	66.9	97.2±5.1	12.82±0.14	1.42 (101)	2.10
OC11	39.788	-13.430	264	Bt-gneiss	Ap (20)	5.70	380	16.46	1098	15.61	9497	97.9	67.8±4.7	-	-	2.09
BB056	38.865	-13.430	515	Phenocryst granite	Ap (25)	6.52	662	13.25	1345	15.61	9497	91.2	96.2±5.8	-	-	2.05
RS0407	36.195	-13.431	621	Mangeritic gneiss	Ap (10)	6.94	137	14.75	291	16.11	6652	64.6	90.7±10.7	-	-	1.87
BB054	40.001	-13.459	245	Syenitic gneiss	Ap (18)	10.39	401	9.38	362	16.07	6652	99.1	211±19.5	-	-	1.81
					Ti (20)	47.31	1356	16.64	477	20.45	6809	69.2	407.4±24	-	-	-
					Zr (22)	78.17	2049	39.94	1047	17.63	8333	95.9	201.1±9.3	-	-	-
BB048	39.891	-13.470	280	Felsic granulite	Ap (19)	3.36	211	4.40	276	16.11	6652	78.7	146.7±15.8	-	-	2.40
ET0410	36.144	-13.475	790	Charnockite	Ap (20)	10.95	838	23.09	1766	16.13	6652	8.2	92.1±7.2	-	-	2.17
BB016	38.222	-13.486	621	Foliated granite	Ap (20)	17.01	357	13.53	284	16.24	6652	83.8	241.5±23.7	-	-	1.99
					Ti (13)	144.97	1147	54.86	434	21.24	6809	57.8	381.5±23.6	-	-	-
BB055	40.003	-13.491	203	Metapelitic gneiss	Ap (20)	6.10	669	11.45	1255	16.15	6652	6.5	106.3±9.2	10.69±0.28	2.18 (61)	1.74
JS347	40.072	-13.567	221	Granitic gneiss	Ap (16)	15.70	734	34.12	1595	18.52	9497	73.8	101.9±7.4	-	-	2.09
RK67	35.339	-13.607	1196	Syenite	Ap (25)	5.73	439	11.77	901	18.74	8333	72.6	95.3±6.6	-	-	2.35
					Zr (23)	66.45	2138	18.90	608	18.38	8333	99.0	371.7±19.7	-	-	-
TBM159	40.393	-13.649	97	Granitic gneiss	Ap (17)	14.38	1148	14.99	1197	18.80	9823	57.7	213.7±15	10.27±0.25	1.46 (33)	1.96
					Zr (22)	144.11	1678	72.74	847	18.64	8333	10.0	212.5±12.2	-	-	-
RK74	35.507	-13.721	958	Dolerite	Ap (8)	33.91	498	79.05	1161	18.35	9823	81.1	94.1±7.4	-	-	1.88
RK76	35.483	-13.713	1062	Granite	Ti (10)	126.73	731	45.42	262	20.34	6809	83.5	385.5±29.4	-	-	-
JS71	35.436	-13.892	1202	Granite	Ti (20)	69.80	1686	20.82	503	20.12	6809	28.4	454.6±26.9	-	-	-
					Zr (26)	85.73	2146	25.89	648	18.71	8333	100.0	356.7±18.6	-	-	-
TBM157	40.378	-13.827	199	Qz-fsp gneiss	Zr (25)	140.97	2815	72.81	1454	18.74	8333	91.2	211.3±8.8	-	-	-
					Ap (20)	53.53	1499	82.56	2313	18.40	9823	30.4	142.2±9.4	12.19±0.15	1.56 (106)	2.26
BB046	39.451	-13.918	296	Augengneiss	Zr (11)	142.73	843	81.95	484	17.97	6809	99.0	182.7±11.5	-	-	-
PND92	36.868	-14.097	665	Granitic gneiss	Ap (24)	10.18	679	11.93	796	15.61	9497	74.9	165.9±10.6	-	-	2.12
RK195	35.659	-14.140	995	Charnockitic gneiss	Ap (20)	68.32	1872	81.75	2240	18.74	9823	0.1	185.5±13.8	11.62±0.20	1.98 (103)	2.09
RK39	36.909	-14.254	648	Mangeritic gneiss	Ap (18)	15.71	1088	23.40	1621	18.86	9823	4.1	153.2±11.7	10.31±0.25	1.83 (52)	1.83
RT557	38.940	-14.317	358	Metapelitic gneiss	Ap (19)	17.49	855	38.09	1862	17.45	9823	62.9	95.8±6.8	-	-	2.15
RT515	38.259	-14.522	472	Leucogneiss	Ap (17)	35.00	1005	78.70	2260	17.39	9823	7.2	92.1±6.8	-	-	2.21
BB102	37.802	-14.587	561	Granitic gneiss	Ap (20)	15.01	1227	26.35	2154	16.22	9823	3.5	111±8.	11.52±0.19	1.92 (102)	2.10
RT582	37.061	-14.632	520	Syenitic gneiss	Zr (22)	201.91	1749	66.49	576	17.73	8333	98.9	311.1±17.1	-	-	-
RK20	36.273	-14.726	659	Quartz Mangerite	Ap (20)	26.70	834	29.39	918	16.20	6652	86.3	174.9±13.1	11.06±0.22	1.98 (80)	2.53
RK292	36.506	-14.808	572	Banded granulite	Ap (20)	15.38	536	15.04	524	18.91	6817	74.9	229±19.3	10.67±0.27	1.73 (39)	2.00
RK45	36.932	-14.832	606	Quartz mangerite	Ap (20)	13.45	752	46.26	909	18.63	9823	53.2	183.6±14.1	11.13±0.18	1.88 (100)	1.98
					Zr (22)	44.04	1266	23.07	663	18.21	9823	24.2	203.5±12	-	-	-
RK243	36.750	-14.921	595	Biotite-granite	Ap (16)	4.64	310	10.33	690	18.69	9823	66.2	100.4±8.9	-	-	1.63
PND40	36.537	-14.928	659	Granite	Zr (19)	171.27	1368	91.52	731	18.44	8333	9.3	203.2±12.9	-	-	-

Sample	E-Long. [Dec. °]	S-Lat. [Dec. °]	Elev. [m]	Lithology	Mineral (# Gr.)	ρ_s [$\frac{10^5}{cm^{-3}}$]	N_s (#)	ρ_i [$\frac{10^5}{cm^{-3}}$]	N_i (#)	ρ_d [$\frac{10^5}{cm^{-3}}$]	N_d (#)	χ^2 [%]	C. Age ±1σ [Ma]	MTL ±1σ [μm]	S_D (# TL)	D_{par} [μm]
Within and south of the Lurio Belt																
OC47	39.898	-13.309	304	Migmatic gneiss	Ap (20)	21.50	1242	21.50	2909	15.61	9497	5.9	83.9 ±4.7	12.56±0.15	1.41 (95)	2.07
OC60	40.027	-13.334	265	Granitic gneiss	Ap (22)	13.21	1203	28.55	2600	15.61	9497	9.9	90.1 ±5	12.83±0.15	1.57 (103)	1.94
RV31	40.239	-13.398	200	Tonalitic gneiss	Ap (20)	20.85	1323	35.14	2230	19.17	4911	76.8	135.6 ±9.1	13.40±0.15	1.44 (91)	2.41
RV35	40.350	-13.417	134	Bt-gneiss	Ap (20)	5.29	550	14.68	550	18.44	4911	71.0	79.5 ±6.1	12.40±0.28	1.60 (32)	2.34
BB062	40.005	-13.510	117	Pegmatite	Zr (15)	90.03	1818	55.76	1527	18.41	8333	78.2	173.6 ±8.0	-	-	-
OC39	40.048	-13.580	236	Granodioritic gneiss	Ap (20)	17.34	1151	39.01	2589	18.57	6817	18.0	98.8 ±6.8	13.02±0.20	1.65 (102)	5.15
OC40	40.041	-13.585	261	Bt-gneiss	Ap (20)	5.84	575	13.34	1313	15.61	9497	97.9	85.7 ±5.3	-	-	2.20
TBM107	39.666	-14.000	358	Phenocryst granite	Ap (26)	3.90	488	8.68	1087	15.61	9497	70.6	87.8 ±5.8	-	-	2.090233333
					Zr (21)	169.50	2355	100.48	1396	18.72	8333	31.1	183.6 ±8.6	-	-	-
BB096	38.907	-14.350	384	Calc-silicate gneiss	Ap (20)	20.16	951	39.80	1878	16.09	6652	20.2	97.8 ±7.1	11.43±0.19	1.93 (100)	1.86
					Ti (20)	97.66	2277	35.68	832	20.40	6809	55.2	379.5 ±18.3	-	-	-
					Zr (23)	136.50	3148	74.97	1729	18.74	8333	96.0	198.8 ±8	-	-	-
RT515	38.259	-14.522	472	Leucogneiss	Zr (8)	107.98	577	68.12	364	18.28	8333	46.4	169.3 ±12.3	-	-	-
RV47	40.410	-14.828	172	Biotite gneiss	Ti (15)	51.96	878	15.86	268	20.85	3463	38.3	459.9 ±36.7	-	-	-
RV46	39.983	-14.889	204	Gneiss	Ap (20)	14.49	687	37.41	1774	15.61	9497	37.9	75.8 ±4.4	-	-	2.18
RV44	40.224	-14.910	140	Tonalitic gneiss	Ti (22)	73.33	1316	27.36	491	20.00	6809	37.8	366.2 ±23.1	-	-	-
RT523	38.517	-14.944	698	Granitic gneiss	Ti (13)	8.76	253	24.10	696	16.21	6652	0.1	73.9 ±9.8	-	-	1.98
RV51	39.704	-15.002	291	Granitic gneiss	Ti (20)	33.33	1206	15.67	567	20.84	3463	3.5	302.3 ±21.5	-	-	-
RV52	39.551	-15.074	326	Metapelitic gneiss	Ti (20)	67.96	1761	30.37	787	20.84	3463	13.3	317.6 ±17.7	-	-	-
JJ259	36.857	-15.456	759	Phenocryst granite	Ap (15)	21.28	639	70.26	2110	16.08	6652	3.9	58.5 ±4.8	11.23±0.19	1.96 (103)	2.28
RT78	35.462	-16.246	-	Augen gneiss	Ti (21)	44.90	1015	19.60	443	21.30	6809	90.3	332.9 ±20.7	-	-	-
					Ap (20)	7.95	417	21.62	1134	16.07	6652	63.0	70.8 ±5.7	-	-	2.06

The results of inverse modeling were used to constrain cooling rates for several time spans related to cooling events. For a significant interpretation all good fitting paths were extracted from the "HeFTy" program [Ketcham, 2005] and a mean cooling rate and the associated standard deviation was computed.

To visualize a continuous graphical representation as age distribution maps of the thermochronological data, the titanite and apatite FT age data sets were interpolated over the investigated interval. We used an inverse-distance-weighting scheme while also propagating the analytical errors for individual FT dates. The resulting age-distribution maps allow only confident inference on a scale twice as large as the sampling area (with highly irregular sample distribution). Note that the results are not very different from commercial solutions (e.g., as provided in GIS-packages).

4. Thermochronological data set

We present 18 new titanite, 18 zircon and 60 apatite FT ages and review the FT dataset from south of the LB reported by Daszinnies [2006] and Daszinnies et al. [2009]. The new data are mainly from samples located north of the LB (Figure 2) but additional results from samples located south of the LB are presented together with the published dataset. To assure data quality, the FT ages are only reported of samples where more than 5 grains could be dated (including published data). Titanite FT ages from 43 samples vary in age between ∼578 and 219 Ma and zircon FT ages between ∼386 and 169 Ma. Apatite FT dating of 142 samples (Table 1, Daszinnies [2006]) gave ages ranging between ∼326 and 59 Ma. The mean track lengths (MTL) of apatite FTs are reported when more than 30 track lengths could be measured. MTLs vary between 14.5 ± 0.2 μm and 10.3 ± 0.3 μm (including published data). Some titanite, zircon and apatite FT ages failed the χ^2-test (Table 1). Different age components, indicated by mineral specific habitus or varying D_{par} values, could be recognised and possibly short termed thermal events, e.g., circulating hot fluids could have caused χ^2-failure. However, for some samples this was not possible and here the failure of the χ^2-test is mainly related to ^{238}U and ^{235}U zoning (Figure 3) which can lead to an extra Poisson error. The titanite and zircon FT data show no significant correlation in the age-elevation diagram (Figure 4a). The majority of the ages cluster between ∼400 and 200 Ma, indicating cooling through the titanite and zircon PAZ during this time interval. Titanite and zircon FT ages plotted against the latitude (Figure 4b) show a clear trend with ages younging towards the south. Thus, an older (∼450-310 Ma) titanite FT age group from samples located north of the LB can be broadly separated

from a younger group (∼320-220 Ma) south of the LB (Figures 4b, 5a). This relationship also holds for the apatite FT ages (Figures 4c, 5b). The thermochronological results north and south of the LB suggest the belt may separate two different tectono-thermal domains (Figures 4, 5). We therefore report the data from the two domains separately.

4.1. Thermochronological results north of the Lurio Belt

Titanite FT ages north of the LB range from 578 ± 36 and 310 ± 30 Ma and are older than their corresponding zircon FT ages which varying between 386 ± 21 and 203 ± 13 Ma (Table 1). Apatite FT ages range from 326 ± 43 Ma to 91 ± 11 Ma. MTL range from 11.62 ± 0.20 to 10.27 ± 0.25 μm with associated standard deviations between 2.18 and 1.46 μm. Mean D_{par} values are between 3.95 and 1.50 μm (Table 1). The apatite FT ages show a diffuse age increase with elevations (Figure 4c). The majority of the samples taken from elevations below 900 m show an inflection at ∼160 Ma, corresponding to samples taken at the margins of the Rovuma and Mozambique basins which do not follow the general trend (Figures 4c, 5b). The apatite FT age vs. MTL suggests a "half boomerang" shape. Samples with MTL longer than 13 μm have apatite FT ages between 158 ± 11 Ma and 136 ± 10 Ma (Figure 4d). The modelled cooling paths of nine samples indicate different phases of accelerated cooling. Samples JS-109 and RK292, located in the NW sector of the working area (Figure 2) show the oldest cooling step into the apatite PAZ. Sample JS109 cooled into the 110-70 °C temperature range between 480 and 400 Ma and best fit paths indicate a mean cooling rate of 2.2 ± 0.5 °CMyr^{-1}. Subsequently, the sample remained for a prolonged time (420 to 35 Ma) in the same temperature field, only reaching the surface environment between 35 Ma and the present (Figure 6). For sample RK292 the timing of entering the PAZ is relatively unconstraint, but during the 220-60 Ma episode the sample remained in the colder part of the PAZ until cooling to surface conditions started (Figure 6). Samples BB016, RV 14, RV 15, RV 16, RV 18 and RV 25 revealed a cooling step from the zircon FT into the apatite FT PAZ during the 240-140 Ma episode. The good-fitting t-T paths of samples located near the eastern margin cover the time between 200-140 Ma and give cooling rates from 1.75 ± 0.3 to 1.25 ± 0.5 °CMyr^{-1} (Figures 6, 7).

4.2. Thermochronological results from within, and south of the Lurio Belt

Four dated titanite FT samples gave ages between 460 ± 37 Ma and 302 ± 22 Ma and 26 samples reported by Daszinnies et al. [2009] have titanite FT ages varying between 378 ± 40 Ma and 219 ± 24 Ma. From all samples only RT51 failed the χ^2-test (Table 1, and Table 3

in Daszinnies et al. [2009]). All titanite FT ages are older than their corresponding zircon FT ages which vary between 213 ± 12 Ma and 169 ± 12 Ma (Table 1). Apatite FT ages are between 147 ± 16 Ma and 59 ± 5 Ma. The MTL vary between 14.50 ± 0.20 and 11.23 ± 0.19 μm with associated standard deviations from 2.70 to 0.70 μm. Etch pit measurements yielded mean D_{par} values between 5.15 and 1.10 μm (Table 1, and Tables 6.1, 6.2, 6.3 in Daszinnies [2006]).

The apatite FT ages from this area show no systematic relationships with sample elevation and MTL (Figures 4c, 4d). A broad age scatter between ∼170-60 Ma occurs at all topographic levels with MTL varying between ∼13.5-11.5 μm (Figure 4d). The apatite FT ages increase with larger D_{par} values (Figure 4e) indicating compositional control on the annealing temperature [e.g., Barbarand et al, 2003]. Two modelled t-T paths from samples RV31 and BB062 located at the eastern margin of the LB yielded different cooling patterns (Figures 6, 7). Sample RV31 shows a similar cooling pattern to samples from the eastern margin north of the LB with an enhanced cooling during the period 180-90 Ma. The good fitting t-T paths indicate a mean cooling rate of 1.7 ± 0.6 °CMyr^{-1}. In contrast, sample BB062 cooled later (125-60 Ma) from the zircon PAZ into the 110-100 °C part of the apatite PAZ giving a cooling rate of 1.2 ± 0.4 °CMyr^{-1}. Cooling from ∼95 °C to surface conditions occurred during the last 40 Ma (Figure 6). Zircon FT ages and modelled apatite FT data of sample TBM107 indicate a cooling step from 200 to 80 °C during 200-140 Ma indicating a mean cooling rate of 1.5 ± 0.5 °CMyr^{-1}. Thereafter, the sample remained in the temperature range ∼80-70 °C until final cooling to surface conditions started at ∼60 Ma (Figure 6).

4.3. Fission track age distribution maps

In general, the titanite FT ages (Figure 5a) show a N-S age decrease with a separation of older from younger ages approximately along the 15 °S latitude-line. This trend is well defined in the western part where titanite ages drop along this latitude line from ∼500 Ma to <250 Ma. In the eastern part, this age trend is not well documented probably due to the lack of data in the northern part. North of 15 °S along an E-W profile the titanite FT ages show a moderate age decrease from ∼500 Ma to ∼380 Ma. A lense of older ages (∼450-400 Ma) at 14 °S/40.5 °E intercepts this trend. South of 15 °S, in the center of the working area, the youngest titanite FT ages (∼230 Ma) are dated. From the spot of youngest ages the titanite FT ages increase laterally to ∼320 Ma (Figure 5a). The apatite FT age distribution is characterised by a general age decrease from ∼250-200 Ma in the NW part of the working area to ∼130-80 Ma on the margins of the old apatite FT domain (Figure 5b). Directly at the
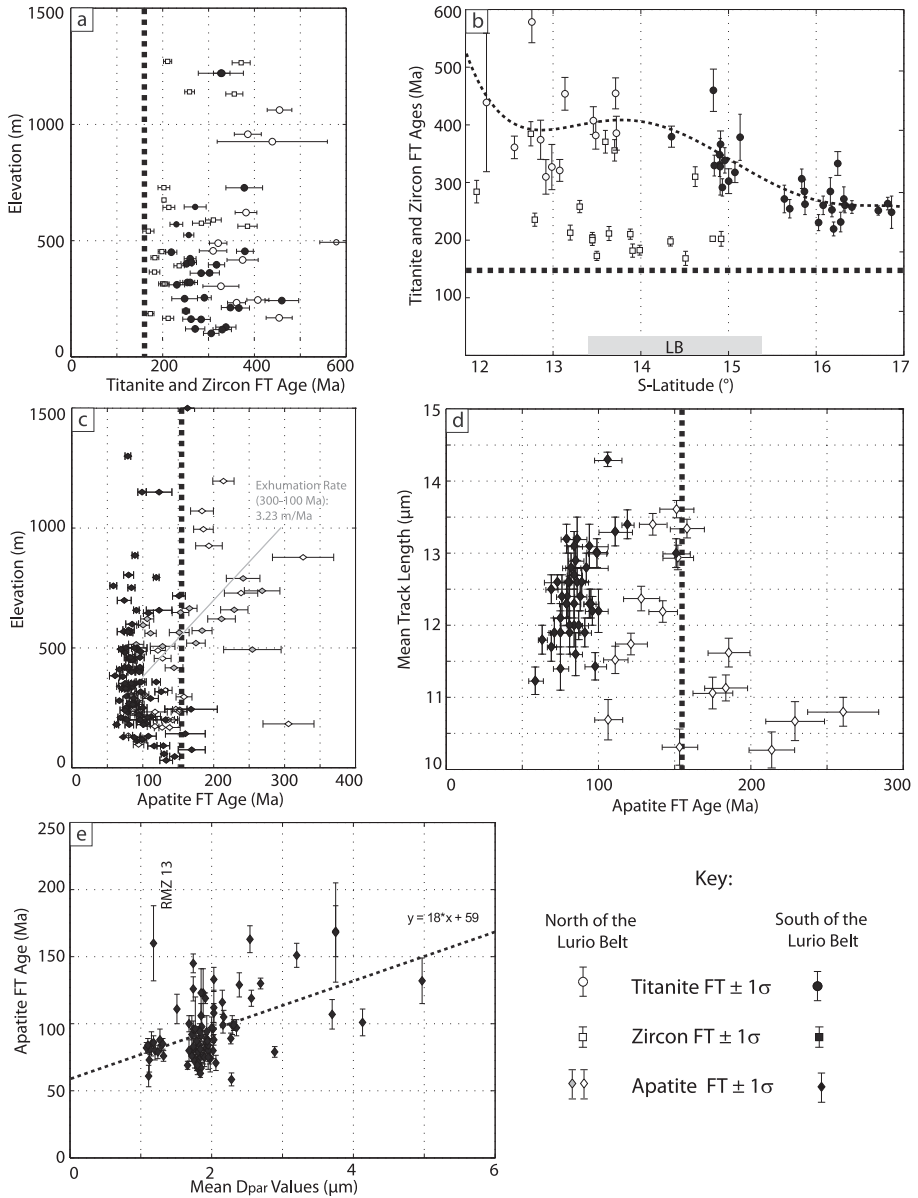
Figure 4: Relationship between FT ages, sample elevation, latitude (in degrees south), MTL and mean D_{par} value. Data are from this study and from Daszinnies [2006] and Daszinnies et al. [2009] a) Titanite and zircon FT ages show a diffuse age spread with elevation. b) Titanite FT ages show a sigmoidal age decrease towards the south. All zircon FT ages are younger than the titanite FT ages and also show younging towards the south. LB:Lurio Belt c) Apatite FT ages are older north of the LB and depict in part an age increase with elevation. Apatite FT ages from an pseudo vertical profile of an unfaulted block show an age increase with elevation (grey symbols). The linear regression (grey line) was used to calculate an exhumation rate of ~ 3.23 mMyr^{-1}. In contrast, samples from south of the Lurio Belt (LB) have apatite FT ages around 100 Ma at all elevation levels. d) MTL plotted against the apatite FT age revealed a "half boomerang" shape for samples located north of the LB. e) D_{par}-values vs. apatite FT age from samples taken south of the LB show an age increase with increasing D_{par}-values. Thick dashed black lines indicate the age of the oldest seafloor anomalies. Thin dashed black lines show fitting regressions.
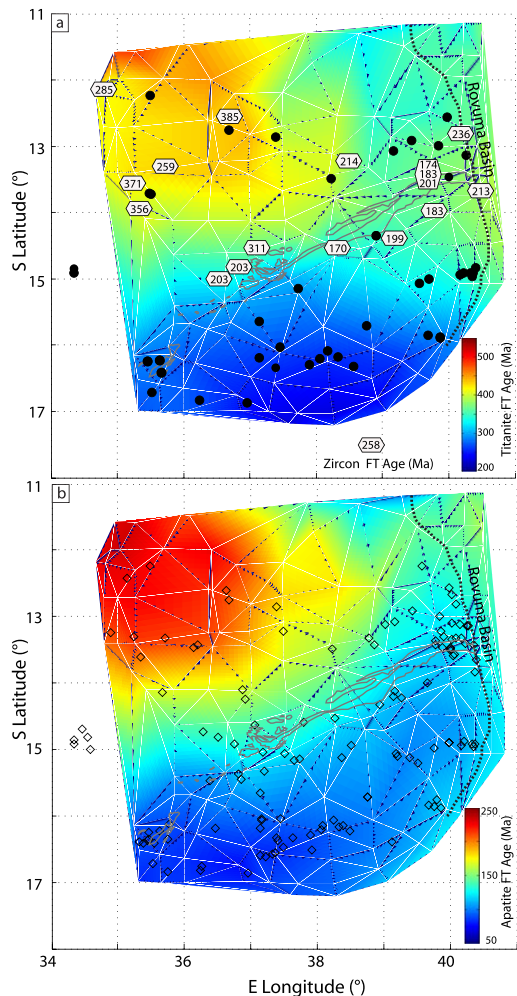
Figure 5: Fission track age distribution maps for northern Mozambique a) Titanite FT ages with zircon FT ages b) Apatite FT age distribution. Grey line indicates the Ocua Complex containing the Lurio Belt (LB).

basement/basin boundary are domains with older apatite FT ages (∼140 Ma) surrounded by younger ones (Figure 5b).

5. Discussion

All FT ages with the exception of one titanite FT age (RK106), are younger than the Lower Ordovician metamorphism [Bingen et al., 2009]. Therefore, our new thermochronological results constrain the post-orogenic cooling history of northern Mozambique from Lower Ordovician to Recent times. In the following section the post-Ordovician basement cooling history, as revealed by the FT data, is discussed in detail.

5.1. Cooling of N Mozambique after peak metamorphism

In the eastern LB, the latest metamorphic event which took place between ∼570 and 530 Ma [Bingen et al., 2009] reached temperatures of ∼950 °C [Engvik et al., 2007]. Thereafter the rocks cooled to surface conditions. The rate of cooling was variable due to local differential erosion in response to local heterogeneous extensional forces e.g., shown by the varying titanite FT ages north of the LB (578 Ma to 310 Ma), and south of the belt (460 Ma to 219 Ma). The titanite FT and some apatite FT ages north of the LB appear to have not been affected by post Pan-African extension. Accordingly, these data can well constrain the subsequent post Pan-African thermal evolution, without the complication of later extensional tectonic events. Inverse modelled t-T paths of sample JS109 revealed a relatively slow mean cooling rate of 2.2 ± 0.5 °C Myr^{-1} for the 480-420 Ma period (Figure 7) and may represent a general trend for the crust north of the LB. In contrast, Ar-Ar hornblende and biotite ages from basement samples south of the LB suggest higher rates (∼11-7 °CMyr^{-1}) of rock cooling during the 500-450 Ma period [Daszinnies et al., 2009]. From this, we can infer that the area south of the LB stayed at a higher temperature longer than in the north due to the widespread intrusion of post-orogenic granitoids between 530 and 490 Ma and associated sillimanite grade metamorphism [Macey et al., 2007, Jacobs et al., 2008, Thomas et al., 2010]. Subsequent thermal relaxation after this magmatic episode can explain the higher cooling rates. As to the origin of the granitoids, which are largely restricted to the Nampula Complex, south of the LB, a model of late orogenic delamination of the crustal root in this part of the East-African Orogen has been proposed [Jacobs and Thomas, 2004, Jacobs et al., 2008]. Such a delamination process would have had a significant impact on the later thermal evolution of the crust south of the LB with probably higher cooling rates following delamination, associated rapid rock uplift and denudation. However, the cooling rates for the areas on each side of the LB were calculated with different thermochronological methods sensitive to variable temperatures (north: ∼300-60 °C, south: ∼500-300 °C), and thus they record cooling through different crustal levels.
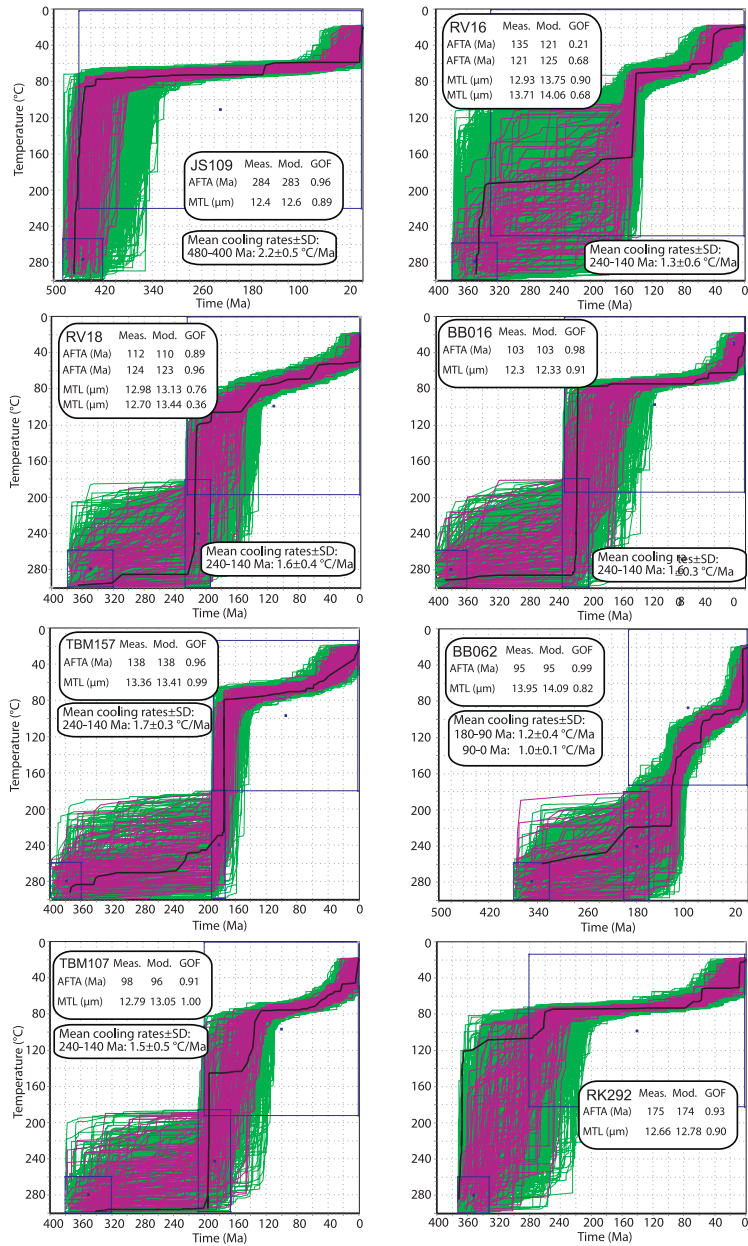
Figure 6: Modelling results for apatite FT data from the basement of northern Mozambique. Green, purple and black lines represent acceptable, good and best fitting time-temperature paths. For the best fitting cooling path, statistics are given. The blue boxes are time-temperature constraints indicated by titanite FT ages, zircon FT ages and present surface temperatures. The statistical fitting parameters and the calculated cooling rates derived from the good fitting paths are given in the insets. Abbreviations: AFTA: Apatite Fission Track Age, GOF: Goodness Of Fit, Meas.: Measured, Mod.: Modelled, MTL: Mean Track Length. Note that MTL are given for c-Axis projected length. Cooling rates, calculated using the slope of the good fitting t-T paths, for different periods are given.
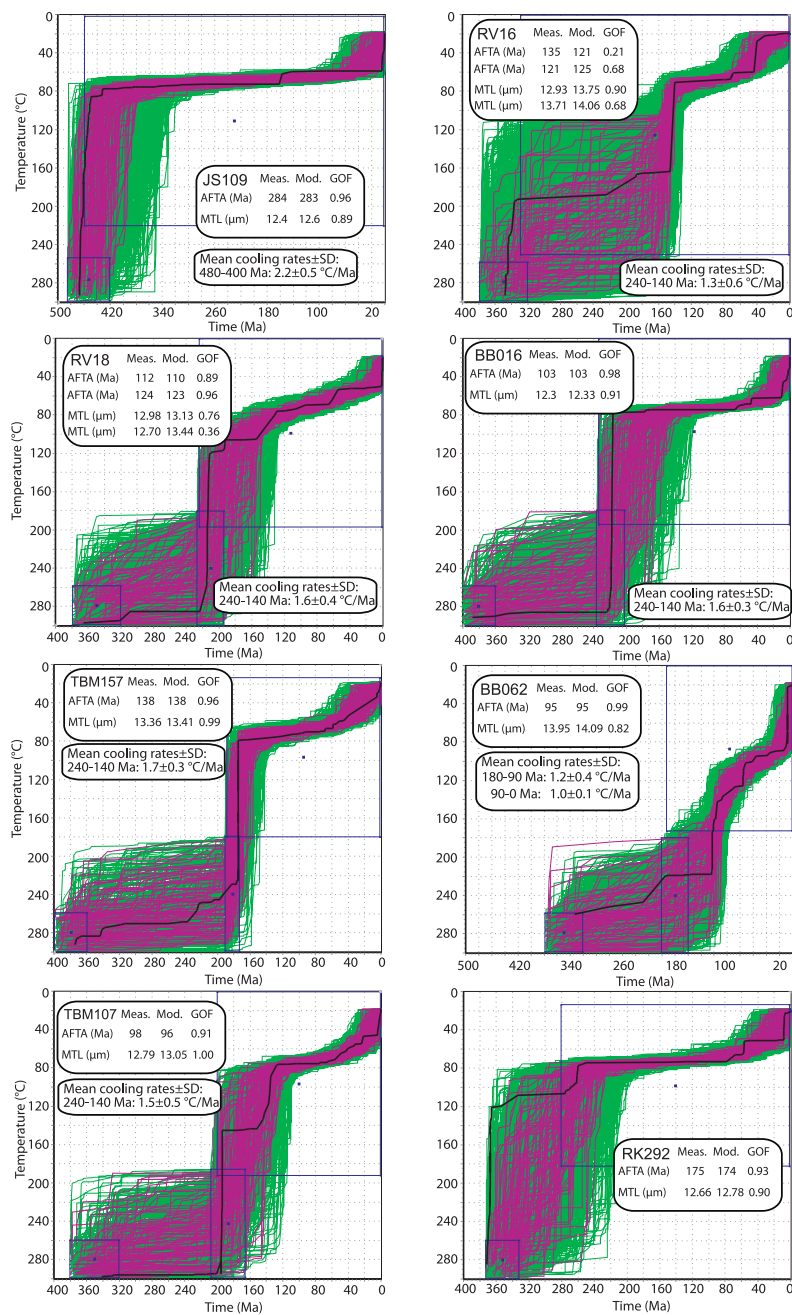
Figure 7: Modelling results for apatite FT data from the faulted basement/basin margin of the Rovuma Basin. Locations are given in Figure 10. For abbreviations and description see Figure 6. The best fit and good fitting t-T paths models from every sample were used to extract cooling rates for the 180-90 Ma and 90-0 Ma episodes.

5.2. The margin evolution of N Mozambique during Gondwana break-up

In the study area, three landscape-forming processes occurred contemporaneously. These are (1) rifting along Lake Malawi, since the late Palaeozoic, with deposition of rift-related sediments within the lake [e.g., Catuneanu et al., 2005]. (2) The opening of the Rovuma transform basin with deposition of a thick on-land sedimentary cover at the eastern coastal margin. (3) Passive margin evolution with final Gondwana fragmentation and sea-floor spreading with formation of oceanic crust along the southern continental margin [Salman and Abdula, 1995], (Figure 1).

5.2.1. Permo- Carboniferous stage

Crustal extension within Gondwana started during the Permo-Carboniferous accompanied by the opening of intracontinental rift basins [e.g., Catuneanu et al., 2005]. Seismic data suggests that Karoo- aged deposits underlie the Early Jurassic sediments in the Rovuma and Mozambique Basins (Figures 1, 2). The effect of this rift episode on the margin evolution is unclear and not revealed by the apatite FT data which is masked by later tectonic processes. However, a combined Ar-Ar and titanite FT study by Daszinnies et al. [2009] indicated that titanite FT ages decrease from 378-327 Ma to 284-219 Ma from the LB towards the southern continental margin. This age trend is interpreted as the erosional response to a Permo-Carboniferous rift shoulder which developed between central Dronning Maud Land (Antarctica) and northern Mozambique. This age distribution is interpreted similar to the apatite FT age pattern along rifted continental margins where the erosion of an escarpment led to a characteristic age pattern. Therefore, FT ages are equal to or less than the age of rifting along the riftward side of the escarpment and older in the hinterland [e.g., Gallagher et al., 1998; Braun et al., 2006]. The new titanite FT ages show a sigmoidal age decrease along a north-south profile across the study area with a significant age drop at 15.2 °S, ~215 km north of the southern continental margin and ~70 km south of the LB (Figures 2, 4). In northern Mozambique, the ~450-310 Ma titanite FT age group lies within the rift hinterland and the younger group (~320-220 Ma) a potential rift-ward side with highest amounts of denudation and isostatic rebound [see Daszinnies et al., 2009]. Thus, our titanite FT ages south of ~15.2 °S give a minimum age for the erosional response due to rifting between Dronning Maud Land and Mozambique at ~258 ± 11 Ma (weighted mean age of 19 titanite FT ages). During the late Carboniferous to early Triassic, large volumes of terrigenous sediments were deposited within Gondwanan rift basins, such as, for example in Kenya, Tanzania and Madagascar [Catuneanu et

al., 2005]. Likewise, titanite, apatite FT and apatite (U-Th)/He studies from the conjugate rift shoulder in Dronning Maud Land suggest a Permo-Carboniferous period of relative rapid cooling as a consequence of the opening of an intracontinental rift between East Antarctica and Mozambique [Emmel et al., 2007, 2009].

5.2.2. Opening of the Rovuma Basin

In northern Mozambique, Mesozoic Gondwana break-up caused rifting and passive margin evolution with an onshore erosional response which is most convincingly recorded by the apatite FT data. For the samples located north of the LB the relationships between apatite FT age, sample elevation and MTL indicate an change in rock cooling rates at ~150-160 Ma, expressed as an inflection in the age-elevation regression line and a half-boomerang shape in the MTL vs. apatite FT age diagram (Figures 4c, 4d). The timing of increased cooling rate is contemporaneous with the age of the oldest seafloor anomalies M25 (158 Ma) in the Mozambique Basin (Figure 4c). The initial rifting and drifting phase was especially pronounced in the basement adjacent to the sedimentary basins (Figures 1, 8, 9). From the Rovuma Basin towards the hinterland, within a distance of ~30 km inland, large strike-slip faults have been mapped, as revealed by digital elevation models (Figure 8) and aeromagnetic data [Norconsult, 2007]. Consequently, the apatite FT data set from the faulted and unfaulted basement zones must be discussed separately because large scale displacement along faults (Figure 8), thermal overprinting by burial heating and circulating hot fluids can cause annealing or conservation of FTs in apatites. This can explain the large scatter in apatite FT ages obtained from samples located directly at the basin margins (Table1, Figure 5b). Along the W margin of the Rovuma Basin, the apatite FT data reflect erosional response to faulting and give the best time estimates for the beginning of the transform movements and the separation of Mozambique from eastern Gondwana (Figure 1). Modelled t-T paths suggest a cooling step at 200-170 Ma which pre-dates the oldest magnetic seafloor anomalies by >12 Myr. This age constraint is in good agreement with the syn-breakup strata in the Morondava Basin (SW Madagascar) where the Toarcian to Aalenian (~190-175 Ma) Andafia Formation dates the beginning of the Madagascar/India/East Antacrtica separation from East Africa [Geiger et al., 2004]. Additionally, a detrital apatite FT study of middle Jurassic sedimentary rocks (174-156 Ma) in the southern Morondava Basin indicate an inversion of Karoo-aged basins and re-deposition into the Jurassic basin as a response to rift migration during the separation of Madagascar from East-Africa [Emmel et al., 2006, 2008]. Along the Rovuma Basin margin, dextral strike-slip faults and many normal faults and joints are ob-
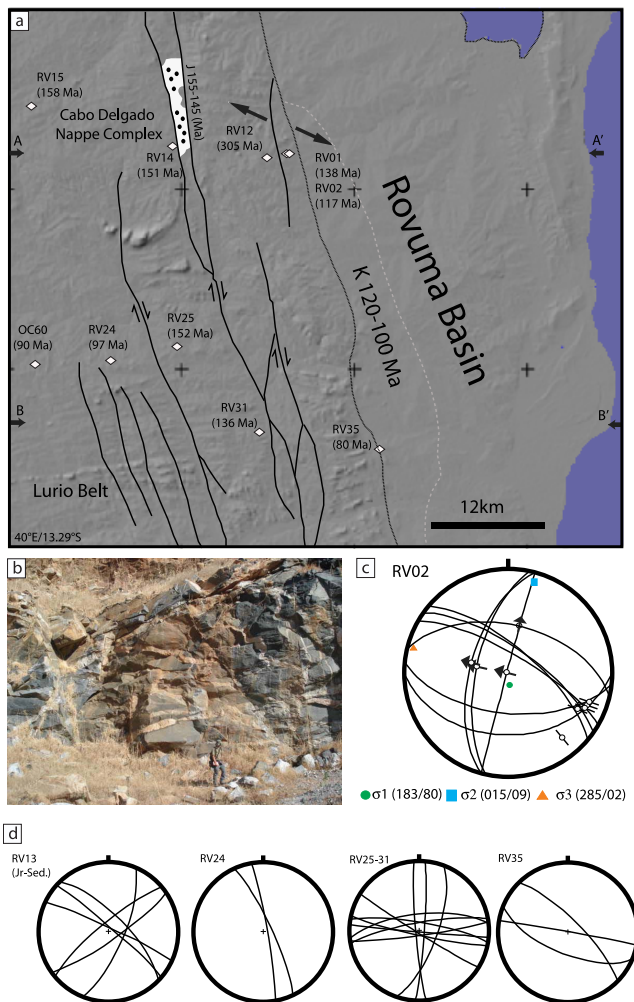
Figure 8: Digital elevation model (SRTM data-set) and brittle structures at the margin of the Rovuma Basin with apatite FT ages. b) Photograph showing the brittle structures at outcrop RV02, W margin of the Rovuma Basin. c) Angelier plot of strike slip data from RV02 whereby the fault planes are given as great circles and the direction of hanging wall movement as poles. The palaeostress was calculated using the dynamic Right Dihedra method [Angelier and Mechler, 1977] and the numerical dynamic analysis [Spang, 1972] with the computer program TectonicsFP [Reiters and Acs, 1996]. Both methods revealed very similar results. c) Stereonet projections of joints from specific outcrops.

served (Figures 8a-c). The strike-slip faults can be traced in digital elevation models because they shape the present topography (Figures 8a). Additionally, ∼10 km W of the main Rovuma Basin N-S trending packages of late Jurassic conglomerates (N'Gapa and Rio Mecule Formations) crop out in isolated basins within the metamorphic basement (Figure 8a). Palaeostress analyses from fault strike-slip

data in outcrop RV02 indicate that σ_3 is related to WNW-SES extension (Figure 8c). Combined with the apatite FT data, the structural data argues for the opening of small pull-apart basins along the NNW-SSE trending major strike-slip faults and a conjugate set of E-W striking minor faults during initial tectonics along the Rovuma Basin

margin (Figure 8) as reported by Key et al. [2008]. In order to quantify differential cooling and denudation of the fault-bounded blocks during the Jurassic to Cretaceous ($\sim$180-90 Ma) and the late Cretaceous to present ($\sim$90-0 Ma), we used the results of modelled good fitting cooling paths (Figure 7). To estimate the amount of denudation, we extracted the temperature information from the good fitting t-T paths of specific samples and assumed a geothermal gradient of 20 $\pm$ 5 °Ckm^{-1}. In both profiles the amount of cooling for the 180-90 Ma (157 $\pm$ 51 to 12 $\pm$ 14 °C) period exceeds the amount for the 90-0 Ma (66 $\pm$ 27 to 18 $\pm$ 6 °C) time span (Figure 9). Consequently, the Jurassic-Cretaceous amount of denudation (10.7 $\pm$ 7.5 to 0.7 $\pm$ 2.2 km) is higher than from the late Cretaceous to the present (3.8 $\pm$ 3.7 to 0.5 $\pm$ 1.4 km). Denudation rates along the faulted basement/basin margin are for profile A-A' (Figures 8, 9) between 11 $\pm$ 6 to 0.6 $\pm$ 2 mMyr^{-1} and between 12 $\pm$ 8 to 0.7 $\pm$ 8 mMyr^{-1} for profile B-B' (Figures 8, 9). Most rates are higher than the background erosion at the hinterland of $\sim$3.2 mMyr^{-1} (Figure 4c) indicating that during the period 180-90 Ma, localised tectonic denudation occurred in a narrow zone of faulted segments ($\sim$30 km wide) and local erosion provided terrestrial sediment for small local pull-apart basins and the adjacent Rovuma Basin (Figures 2, 8a).

5.2.3. Passive margin along the Mozambique Basin

South of the LB the apatite FT ages show an exceptionally uniform distribution without normal age increases with elevation or with distance to the continental margins (Figures 4c, 5b). The apatite FT ages vary between $\sim$170 Ma and 60 Ma, with a majority of ages between 130-70 Ma (Table 1 and Tables 6.1, 6.2, 6.3 in Daszinnies, [2006]). This spectrum of apatite FT ages can be explained mainly in terms of one thermo-tectonic episode which affected the apatites with different annealing resistances caused, for example, by variable chemical compositions. Figure 4e shows an increase of apatite FT ages with D_{par} values. The Ketcham et al. [1999] annealing model expands the apatite FT PAZ for apatites with D_{par} values of 5 μm, and an isothermal holding time of 100 Myr, to a high-temperature threshold of 205 °C. Considering variable temperature sensitivities for apatite FT ages obtained from apatites with different D_{par} values, the apatite FT age distribution pattern south of the LB could result from one relatively slow cooling episode, whereby track

accumulation started at different temperatures (e.g., between $\sim$150-100 °C) and samples were located at different palaeo-elevations. Assuming a differential temperature sensitivity of 50 °C and a slow cooling rate of 2 °CMyr^{-1} the compositional affect could cause an age discrepancy of 25 Ma between samples from the same localities and with the same cooling history. However, the majority of modelled t-T paths from Daszinnies [2006] show Cretaceous cooling into or through the apatite PAZ. Only samples from locations along the faulted south and SE basement margin and close to the LB show Jurassic cooling into the PAZ [see Figures 6.6 and 6.10 in Daszinnies, 2006]. This cooling can be explained by pre-Cretaceous tectonics and conservation of old apatite FT in fault bounded blocks (see 6.3.2). The data presented here and in Daszinnies [2006] indicate unusually uniform Cretaceous cooling of a very large area ($\sim$150 000 km2) south of the LB (Figure 5b). This age pattern is hard to explain by surface processes caused by normal rift shoulder erosion and isostatic response. We suggest two different mechanisms for this episode, both of which are related to hypothetical mantle-crust interactions and to inherited different lithospheric properties north and south of the LB.

(1) *Late Jurassic – Cretaceous magmatic underplating and thermal compensation south of the LB.* Several geological observations support this hypothesis: (a) Coeval magmatism. Evidence for Late Jurassic- Cretaceous magmatic activity in northern Mozambique is restricted mainly to the area south of the LB but magmatism was widespread in central Gondwana (see 2.3; Figure 1). (b) Furthermore, a 2D flexural backstripping and gravity model from the southern tip of the northern Mozambiquan margin indicates that newly formed oceanic crust was probably underplated by magmatic material [Watts, 2001]. (c) Magmatic underplating would cause substantial uplift followed by denudation [Cox, 1993; Al Kindi et al., 2003] at a km-scale. Such denudation is recorded by the cooling paths obtained from basement samples south of the LB. (d) Additionally, the Cretaceous was a time of high sediment influx into the Zambezi Delta, contemporaneous with the Cretaceous basement cooling event [Walford et al., 2005]. (e) Following the Cretaceous peak, sedimentation in the Zambezi Delta abruptly declined [Walford et al., 2005].

(2) *Late Jurassic – Cretaceous differential stretching [compare with Dunbar and Sawyer, 1988; Corti and Manetti, 2006].* This hypothesis is based on the assumption that crustal thinning occurred at the present southern margin, while distributed stretching of the mantle lithosphere was located northwards beneath the continental crust up to the LB. Two geological processes could have caused significant lithospheric mantle stretching during extension: previous partial loss of lithospheric mantle, or a deep inherited heterogeneity from earlier regional-scale
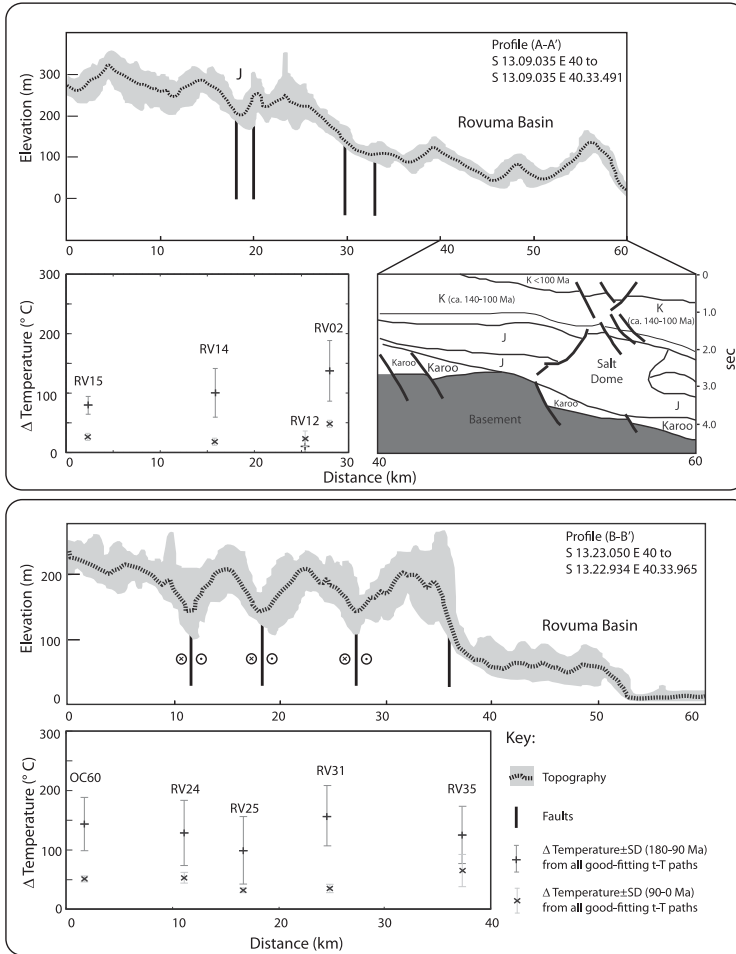
Figure 9: Two topographic parallel (± 500m) cross-sections from the faulted NE basement/basin margin with estimates on differential cooling. Profile locations are shown in Figure 8 and interpreted seismic profile for km 40-60 in cross section A-A' is from Salman and Abdula [1995]. Note that the peak of sedimentation occurred during the Early Jurassic-Early Cretaceous coeval with the main basement rock cooling.

deformation. Jacobs et al., [2008] suggest that during orogenic collapse following the Pan-African collision event there was an early Palaeozoic partial, lithospheric delamination south of the LB. A post-delamination thickness contrast might thus have caused differential lithospheric strength north and south of the LB which was strong enough to stretch only the lithosphere south of the LB.

Such a process would cause relative uplift in the stretched-lithosphere domain (i.e. south of the LB) and relative subsidence in the overlying stretched crust domain of the Mozambique Basin. This model accounts for the parallelism between the LB and the present southern coastal margin (Figure 2) and the comparatively sudden limitation of increased relative cooling by the LB (Figure 5b).
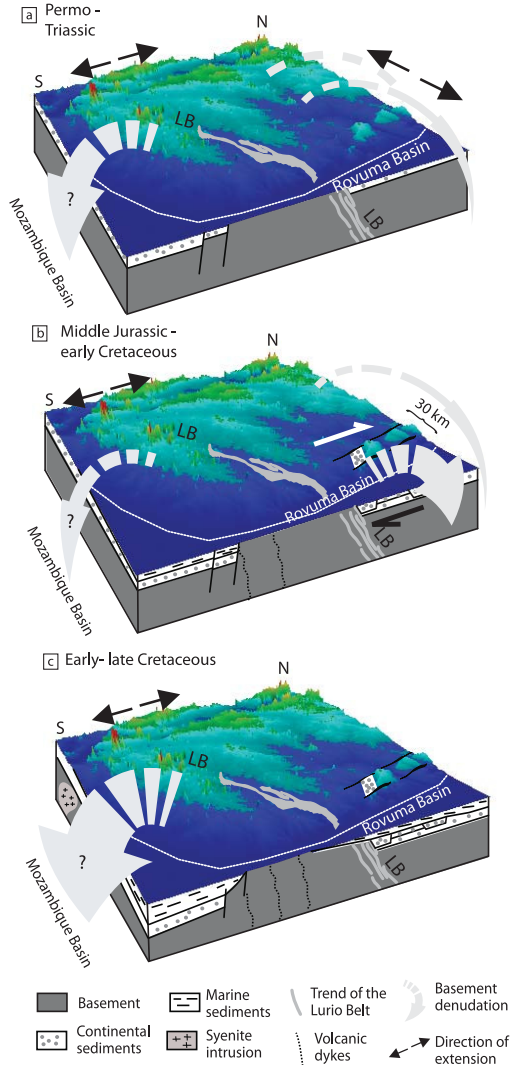
Figure 10: 3D cartoon describing the conceptual model for the Permian to late Cretaceous basement denudation history of northern Mozambique (a-c). The present topography (SRTM data-set) is given and different denudation events are shown with grey arrows (thickness of the arrow indicates the relative degree of denudation). Black arrows show extension directions and dashed thin white line is the present day coastline. Note that the cartoon is not to scale.

6. Conclusions

In this paper, we have presented a conceptual model to constrain the post Pan-African cooling history of an "orogen-passive margin system" in N Mozambique (Figure 10). The model is mainly based on a combined thermochronological dataset supported by structural and sedimentological data. The post-metamorphic basement cooling history is influenced by the opening of the Rovuma and Mozambique Basins from late Carboniferous times (initial intracontinental rift phase) until the present. During the late Carboniferous-Triassic intracontinental rift phase, higher denudation occurred at the southern margin and slow denudation shaped the landscape of the northern part. During the early Jurassic opening of the Rovuma Basin, denudation was localised along major faults. Subsequently, late Jurassic to early Cretaceous volcanic rocks emplaced in the already stretched and fractured parts of the crust during the southward drift of East Gondwana from East Africa. Two tectonic possibilities are proposed, to explain the uniform Cretaceous basement cooling pattern south of the LB, in the hinterland of the Mozambique Basin, one indicating crustal thickening (underplating) and the other thinning (differential stretching). Both scenarios are dependant on inherited lithospheric properties related to older, major tectonic events. The LB is a prominent Pan-African structure that represents a thermochronological boundary which is mimicked by the present drainage pattern. Combined FT data indicate maximum differential exhumation of ∼10 km north and south of the belt. This thermochronological pattern seems to be related to Mesozoic extensional tectonics, which itself might be governed by the pre-break-up crustal architecture. However, within the basement of NE Mozambique oldest rocks (north of the LB) are preserved where lowest Mesozoic-Cenozoic denudation occurred. This has to be taken into account during the interpretation of high temperature sensitive geochronological methods in this critical part of the Gondwana puzzle.

Acknowledgements

References

Angelier, J., Mechler, P., 1977. Sur une méthode graphique de recherche des contraintes principales également utilisable en tectonique et en seismologie: la methode dièdres doits. Bulletin de la Société Géologique France 19, 1309–1318.

Bernet, M., 2009. A field-based estimate of the zircon fission-track closure temperature. Chemical Geology 259, 181–189.

Bingen, B., Jacobs, J., Viola, G., Henderson, I.H.C., Skår, Ø., Boyd, R., Thomas, R.J., Solli, A., Key, R.M., Daudi, E.X.F., 2009. Geochronology of the Precambrian crust in the Mozambique belt in NE Mozambique, and implications for Gondwana assembly. Precambrian Research 170, 231–255.

Boger, S.D., Miller, J.M., 2004. Terminal suturing of gondwana and the onset of the ross-delamerian orogeny: the cause and effect of an early cambrian reconfiguration of plate motions. Earth and Planetary Science Letters 219, 35–48.

Boyd, R., Nordgulen, Ø., Thomas, R.J., Bingen, B., Bjerkgård, T., Henderson, I.H.C., Melezhik, V.A., Sandstad, J.S., Solli, A., Tveten, E., Viola, G., Key, R.M., Smith, R.A., Gonzales, E., Hollick, L., Jacobs, J., Jamal, D., Motuza, G., Bauer, W., Daudi, E., Feitio, P., Manhica, V., Moniz, A., Rosse, D., 2010. The geology and geochemistry of the East African Orogen in NE Mozambique. South African Journal of Geology 113, 87–129.

Brandon, M.T., Roden-Tice, M.K., Garver, J.I., 1998. Late Cenozoic exhumation of the Cascadia accretionary wedge in the Olympic Mountains, NW Washington State. Geological Society of America Bulletin 110, 985–1009.

Braun, J., van den Beek, P., Batt, G., 2006. Quantitative Thermochronology: Numerical Methods for the Interpretation of Thermochronological Data. Cambrige University Press, Cambridge, New York, 258 pp.

Cateanu, O., Wopfner, H., Eriksson, P.G., Cairncross, B., Rubidge, B.S., Smith, R.M.H., Hancox, P.J., 2005. The Karoo basins of south-central Africa. Journal of African Earth Sciences 43, 211–253.

Civitelli, G., Mariani, F., 1984. Estudo geológica do sedimentary da Provincia de Cabo Delgado finalizado a pesquisa de gerso. Unpublished Bulletin BGI, Instituto Naçional de Geologica, Maputo.

Corti, G., Manetti, P., 2006. Asymmetric rifts due to asymmetric Mohos: an experimental approach. Earth and Planetary Science Letters 245, 315–329.

Cox, K.G., 1992. Karoo igneous activity, and the early stage of the break-up of Gondwanaland, in: Storey, B., Alabasterf, A. (Eds.), Magmatism and the cause of continental break-up. Geological Society of London, Special Publication 68, 137-148.

Cox, K.G., 1993. Continental magmatic underplating. Philosophical Transactions of the Royal Society London A 342, 155–166.

Coyle, D.A., Wagner, G.A., 1998. Positioning the titanite fission-track partial annealing zone. Chemical Geology 149, 117–125.

Daly, M.C., Chorowicz, J., Fairhead, J.D., 1989. Rift basin evolution in Africa: the influence of reactivated steep basement shear zones, in: Cooper, M.A., Williams, G.D. (Eds.), Inversion Tectonics. Geolgical Society of London, Special Publications 44, 309-334.

Daszinnies, M.C., 2006. The Phanerozoic thermo-tectonic evolution of northern Mozambique constrained by $^{40}Ar/^{39}Ar$, fission track and (U-Th)/He analyses. Ph.D. thesis. University of Bremen, 227 pp.

Daszinnies, M.C., Jacobs, J., Wartho, J.A., Grantham, G.H., 2009. Post Pan-African thermo-tectonic evolution of the north Mozambican basement and its implication for the Gondwana rifting. Inferences from 40Ar/39Ar hornblende, biotite and titanite fission-track dating, in: Lisker, F., Ventura, B., Glasmacher, U. (Eds.), Thermochronological methods: from palaeotemperature constraints to landscape evolution model. Geological Society of London, Special Publications 324, 317-330, pp. 317–330.

de Wit, M.J., 2003. Madagascar: heads it's a continent, tails itís an island. Annual Review of Earth and Planetary Sciences 31, 213–248.

Dumitru, T., 1991. A new computer-automated microscopic stage system for fission track analysis. On Track 1, 1–7.

Dunbar, J.A., Sawyer, D.S., 1988. Continental rifting at pre-existing lithospheric weaknesses. Nature 333, 450–452.

Duncan, R.A., Hooper, P.R., Rehacek, J., Marsh, J.S., Duncan, A.R., 1997. The timing and duration of the Karoo igneous event, southern Gondwana. Journal of Geophysical Research 102, B8, 18127–18138.

Eby, G.N., Roden-Tice, M., Krueger, H.L., Ewing, W., Faxon, E.H., Woolley, A.R., 1995. Geochronology and cooling history of the northern part of the Chilwa alkaline province, Malawi. Journal of African Earth Sciences 20, 275–288.

Emmel, B., Geiger, M., Jacobs, J., 2006. Detrital apatite fission-track ages in Middle Jurassic strata at the rifted margin of W Madagascar - an indicator for a protracted resedimentation history. Sedimentary Geology 186, 27–38.

Emmel, B., Jacobs, J., Crowhurst, P., Daszinnies, M.C., 2007. Combined apatite fission-track and single grain apatite (U-Th)/He ages from basement rocks of central Dronning Maud Land (East Antarctica) - possible identification of thermally overprinted crustal segments. Earth and Planetary Science Letters 264, 72–88.

Emmel, B., Jöns, N., Kröner, A., Jacobs, J., Wartho, J.A., Schenk, V., Razakamanana, T., Austegard, A., 2008. From closure of the Mozambique Ocean to Gondwana breakup: new evidences from geochronological data of the Vohibory terrane, SW Madagascar. Journal of Geology 116, 21–38.

Engvik, A.K., Tveten, E., Bingen, B., Viola, G., Erambert, M., Feitio, P., de Azavedo, S., 2007. P-T-t evolution and decompression textures of Pan-African high-pressure granulites, Lurio Belt, northeastern Mozambique. Journal of Metamorphic Geology 25, 935–952.

Gallagher, K., Brown, R., Johnson, C., 1998. Fission track analysis and its applications to geological problems. Annual Review of Earth and Planetary Sciences 26, 519–572.

Geiger, M., Clark, D.N., Mette, W., 2004. Reappraisal of the timing of the break-up of Gondwana based on sedimentological and seismic evidence from the Morondava Basin, Madagascar. Journal of African Earth Sciences 38, 363–381.

Gleadow, A.J.W., 1981. Fission track dating methods: What are the real alternatives? Nuclear Tracks and Radiation Measurements 5, 3–14.

Grantham, G.H., Macey, P., Ingram, B.A., Rademeyer, M., Eglington, B., Keidan, H., de Azavedo, S., 2005. The chemistry and age of Karoo-age andesitic lavas along the northern Mozambique coast, in: Pankhurst, R.J., Veiga, G.D. (Eds.), Gondwana 12. Mendoza, Argentina, 183.

Grantham, G.H., Macey, P.H., Ingram, B.A., Roberts, M.P., Armstrong, R.A., Hokada, T., Shiraishi, K., Jackson, C., Bisnath, A., Manhica, V., 2008. Terrane correlation between Antarctica, Mozambique and Sri Lanka: Comparison of geochronology, lithology, structure and metamorphism and possible implications for the geology of southern Africa and Antarctica, in: Satish-Kumar, M., Motoyoshi, Y., Osanai, Y., Hiroi, Y., Shiraishi, K. (Eds.), Geodynamic Evolution of East Antarctica: A Key to the East-West Gondwana Connection. Geological Society of London, Special Publications 308, 91-119.

Green, P.F., 1981. A new look at statistics in fission-track dating. Nuclear Tracks and Radiation Measurements 5, 77–86.

Green, P.F., Duddy, I.R., Gleadow, A.J.W., Tingate, P.R., Laslett, G.M., 1986a. Fission-track annealing in apatite; track length measurements and the form of the Arrhenius plot. Nuclear Tracks and Radiation Measurements 10, 323–328.

Green, P.F., Duddy, I.R., Gleadow, A.J.W., Tingate, P.R., Laslett, G.M., 1986b. Thermal annealing of fission tracks in apatite 1. A Qualitative Description. Chemical Geology 59, 237–253.

Hancox, P.J., Brandt, D., Edwards, H., 2002. Sequence stratigraphic analysis of the Early Cretaceous Maconde Formation (Ruvuma Basin), northern Mozambique. Journal of African Earth Sciences 34, 291–297.

Harrison, T.M., Armstrong, R.L., Naeser, C.W., Harakal, J.E., 1979. Geochronology and thermal history of the Coastal Plutonic Complex, near Prince Rupert, British Columbia. Canadian Journal of Earth Sciences 16, 400–410.

Hurford, A.J., 1990. International Union of Geological Sciences Subcommission on Geochronology Recommendation for standardization of fission track dating calibration and data reporting. Nuclear Tracks and Radiation Measurements 17, 233–236.

Jacobs, J., Bingen, B., Thomas, R.J., Bauer, W., Wingate, M., Feitio, P., 2008. Early Palaeozoic orogenic collapse and voluminous late-tectonic magmatism in Dronning Maud Land and Mozambique: insights into the partially delaminated orogenic root of the East African-Antarctic Orogen?, in: Satish-Kumar, M., Motoyoshi, Y., Osanai, Y., Hiroi, Y., Shiraishi, K. (Eds.), Geodynamic Evolution of East Antarctica: A Key to the East-West Gondwana Connection. Geological Society of London, Special Publications 308, 69-90.

Jacobs, J., Thomas, R.J., 2004. Himalayan-type indenter-escape tectonics model for the southern part of the late Neoproterozoic-early Paleozoic East African- Antarctic orogen. Geology 32, 721–724.

Jamal, D., 2005. Crustal studies across selected geotransects in NE Mozambique: Differentiating between Mozambiquan (~Kibaran) and Pan African events, with implications for Gondwana studies. Ph.D. thesis. Univ. of Cape Town, Cape Town, South Africa.

Jaritz, W., Kreuzer, H., Mueller, P., Harre, W., 1977. Die Vulkanitserien im Küstengebiet von Nordmoçambique. Geologisches Jahrbuch Reihe B: Regionale Geologie Ausland 26, 147–165.

Kent, P.E., Johnstone, J.A.H.D.W., 1971. The geology and geophysics of Coastal Tanzania. Institute of Geological Sciences Geophysical Paper No. 6, Her Majestyís Stationary Office, London, United Kingdom, 101 pp .

Ketcham, R.A., 2005. Forward and Inverse Modeling of Low-Temperature Thermochronometry Data. Reviews in Mineralogy and Geochemistry 58, 275–314.

Ketcham, R.A., Donelick, M.B., Carlson, W.D., 1999. Variability of apatite fission-track annealing kinetics: III. Extrapolation to geological time scales. American Mineralogist 84, 1235–1255.

Key, R.M., Bingen, B., Barton, E., Daudi, E.X.F., Manuel, S., Moniz, A., 2007. Kimberlites in a Karoo graben of northern Mozambique: tectonic setting, mineralogy and Rb-Sr geochronology. South African Journal of Geology 110, 111–124.

Key, R.M., Smith, R.A., Smelror, M., Powell, J.H., Thorsnes, T., Njange, F., Sæther, O.M., Zandamela, E.B., 2008. Revised lithostratigraphy of the Mesozoic-Cenozoic succession of the onshore Rovuma Basin, northern coastal Mozambique. Journal of African Earth Sciences 111, 89–108.

Kohn, B.P., Wagner, M.E., Lutz, T.M., Organist, G., 1993. Anomalous Mesozoic thermal regime, central Appalachian Piedmont; evidence from sphene and zircon fission-track dating. Journal of Geology 101, 779–794.

Kusky, T.M., Abdelsalam, M., Stern, J.S., Tucker, R.D., 2003. Evolution of the East African and related orogens, and the assembly of Gondwana. Precambrian Research 123, 81–85.

Lächelt, S., 2004. The Geology and Mineral Resources of Mozambique. Direcção Nacional de Geologia Moçambique (DNG), Maputo, 515 pp .

Luttinen, A.V., Furnes, H., 2000. Flood basalts of Vestfjella: Jurassic magmatism across an Archaean-Proterozoic lithospheric

boundary in Dronning Maud Land, Antarctica. Journal of Petrology 41, 1271–1305.

Macey, P.H., Ingram, B.A., Roberts, M.R., de Kock, G., Cronwright, M.S., Botha, G.A., Grantham, G.H., Maree, L., Botha, P.M.W., Kota, M., Opperman, R., Haddon, I.G., Rowher, M., Nolte, J.C., 2007. Map explanation of sheets Alto Molócuè, 1537. Murrupula, 1538. Nampula, 1539. Mogincual, 1540. Errego, 1637. Gilé (1638) and Angoche (1639 - 40). Technical Report. National Directorate of Geology, Republic of Mozambique.

Meert, J.G., 2003. A synopsis of events related to the assembly of eastern Gondwana. Tectonophysics 362, 1–40.

Melezhik, V.A., Kuznetsov, A.B., Fallick, A.F., Smith, R.A., Gorokhov, I.M., Jamal, D., Catuane, F., 2006. Depositional environments and an apparent age for the Geci meta-limestones: constraints on the geological history of northern Mozambique. Precambrian Research 148, 19–31.

Nairn, A.E.L., Lerche, I., Iliffe, J.E., 1991. Geology, basin analysis, and hydrocarbon potential of Mozambique and the Mozambique Channel. Earth Science Reviews 20, 81–124.

Norconsult Consortium, 2007. Mineral Resources Management Capacity Building Project, Republic of Mozambique; Component 2: Geological Infrastructure Development Project, Geological Mapping Lot 1; Sheet Explanation: 32 Sheets; Scale: 1/250000, Report No. B6.f. Technical Report. National Directorate of Geology, Republic of Mozambique.

Pinna, P., Jourde, G., Calvez, J.Y., Mroz, J.P., Marques, J.M., 1993. The Mozambique Belt in northern Mozambique; Neoproterozoic (1100 - 850 Ma) crustal growth and tectogenesis, and superimposed Pan-African (800 - 550 Ma) tectonism. Precambrian Research 62, 1–59.

Rahn, M.K., Brandon, M.T., Batt, G.E., Garver, J.I., 2004. A zero-damage model for fission-track annealing in zircon. American Mineralogist 89, 473–484.

Reeves, C.V., de Wit, M.J., Sahu, B.K., 2004. Tight reassembly of Gondwana exposes Phanerozoic shears in Africa as global tectonic players. Gondwana Research 7, 7–19.

Reiter, F., Acs, P., 1996. TectonicsFP. Software for structural geology. Innsbruck University, Austria.

Salman, G., Abdula, I., 1995. Development of the Mozambique and Ruvuma sedimentary basins, offshore Mozambique. Sedimentary Geology 96, 7–41.

Smelror, M., Key, R.M., Smith, R.A., Njange, F., 2008. Late Jurassic and Cretaceous palynostratigraphy of the onshore Rovuma Basin, northern Mozambique. Palynology 32, 63–76.

Spang, J.H., 1972. Numerical method for dynamic analysis of calcite twin lamellae. Geological Society of America Bulletin 83, 467–472.

Stern, R.J., 1994. Arc assembly and continental collision in the Neoproterozoic East African Orogen: implications for the consolidation of Gondwanaland. Annual Reviews Earth and Planetary Sciences 22, 319–351.

Storey, M., Mahoney, J.J., Saunders, A.D., Duncan, R.A., Kelley, S.P., Coffin, M.F., 1995. Timing of hot spot-related volcanism and the breakup of Madagascar and India. Science 267, 852–855.

Takigami, Y., Yoshida, M., Funaki, M., 1999. ^{40}Ar-^{39}Ar ages of dolerite dykes from Sri Lanka. Polar Geoscience 12, 176–182.

Thomas, R.J., Jacobs, J., Horstwood, M.S.A., Ueda, K., Bingen, B., Matola, R., 2010. The Mecubúri and Alto Benfica Groups, NE Mozambique: Aids to unravelling ca. 1 and 0.5 Ga events in the East African Orogen. Precambrian Research 178, 72–90.

Torsvik, T.H., Tucker, R., Ashwal, L., Eide, E., Rakotosolofo, N., de Wit, M.J., 1998. Late Cretaceous magmatism in Madagascar; palaeomagnetic evidence for a stationary Marion hotspot. Earth and Planetary Science Letters 164, 221–232.

Verniers, J., Jourdan, P.P., Paulis, R.V., Frasca-Spada, L., DeBock, F.R., 1989. The Karoo graben of Metangula, northern Mozam-

bique. Journal of African Earth Sciences 9, 137–158.

Viola, G., Henderson, I.H.C., Bingen, B., Thomas, R.J., Smethurst, M.A., de Azavedo, S., 2008. Growth and collapse of a deeply eroded orogen: insights from structural and geochronological constraints on the Pan-African evolution of NE Mozambique. Tectonics 27, TC5009, doi:10.1029/2008TC002284.

Wagner, G.A., Van den Haute, P., 1992. Fission-Track Dating. Ferdinand Enke Verlag, Stuttgart, 285 pp.

Walford, H.L., White, N.J., Sydow, J.C., 2005. Solid sediment load history of the zambesi delta. Earth and Planetary Science Letters 238, 49–63.

Watts, A.B., 2001. Gravity anomalies, flexure and crustal structure at the Mozambique rifted margin. Marine and Petroleum Geology 18, 445–455.

Yoshida, M., Funaki, M., Vitanage, P., 1989. A Jurassic dolerite dyke from Sri Lanka and its palaeomagnetic analysis. Journal Geological Society India 30, 71–76.

Zhang, X., Luttinen, A.V., Elliot, D.H., Larsson, K., Foland, K.A., 2003. Early stages of Gondwana breakup: The 40Ar/39Ar geochronology of Jurassic basaltic rocks from western Dronning Maud Land, Antarctica, and implications for the timing of magmatic and hydrothermal events. Journal of Geophysical Research 108, B9, ECV 7–1 – 7–19.